



RESEARCH ARTICLE

10.1029/2021MS002952

ICON-O: The Ocean Component of the ICON Earth System Model—Global Simulation Characteristics and Local Telescoping Capability

Key Points:

- We describe **Icosahedral Nonhydrostatic Weather and Climate Model (ICON-O)** the ocean component of **ICON-ESM 1.0**, based on the **ICON modeling framework**
- **ICON-O** is analyzed in a globally mesoscale-rich simulation and in a telescoping configuration
- In telescoping configuration **ICON-O** reproduces locally the eddy dynamics with less computational costs than the uniform configuration

Correspondence to:









P. Korn,
peter.korn@mpimet.mpg.de

Citation:

Korn, P., Brüggemann, N., Jungclaus, J. H., Lorenz, S. J., Gutjahr, O., Haak, H., et al. (2022). **ICON-O: The ocean component of the ICON Earth system model—Global simulation characteristics and local telescoping capability.** *Journal of Advances in Modeling Earth Systems*, 14, e2021MS002952. <https://doi.org/10.1029/2021MS002952>

Received 20 DEC 2021

Accepted 14 JUL 2022

P. Korn¹ , N. Brüggemann^{1,2}, J. H. Jungclaus¹ , S. J. Lorenz¹, O. Gutjahr^{1,2} , H. Haak¹ , L. Linardakis¹, C. Mehlmann¹ , U. Mikolajewicz¹, D. Notz^{1,2}, D. A. Putrasahan¹ , V. Singh¹, J.-S. von Storch¹ , X. Zhu^{1,2}, and J. Marotzke^{1,2} 

¹Max Planck Institute for Meteorology, Hamburg, Germany, ²Institute of Oceanography, University of Hamburg, Hamburg, Germany

Abstract We describe the ocean general circulation model **Icosahedral Nonhydrostatic Weather and Climate Model (ICON-O)** of the Max Planck Institute for Meteorology, which forms the ocean-sea ice component of the Earth system model **ICON-ESM**. **ICON-O** relies on innovative structure-preserving finite volume numerics. We demonstrate the fundamental ability of **ICON-O** to simulate key features of global ocean dynamics at both uniform and non-uniform resolution. Two experiments are analyzed and compared with observations, one with a nearly uniform and eddy-rich resolution of ~ 10 km and another with a telescoping configuration whose resolution varies smoothly from globally ~ 80 to ~ 10 km in a focal region in the North Atlantic. Our results show first, that **ICON-O** on the nearly uniform grid simulates an ocean circulation that compares well with observations and second, that **ICON-O** in its telescope configuration is capable of reproducing the dynamics in the focal region over decadal time scales at a fraction of the computational cost of the uniform-grid simulation. The telescopic technique offers an alternative to the established regionalization approaches. It can be used either to resolve local circulation more accurately or to represent local scales that cannot be simulated globally while remaining within a global modeling framework.

Plain Language Summary **Icosahedral Nonhydrostatic Weather and Climate Model (ICON-O)** is a global ocean general circulation model that works on unstructured grids. It rests on novel numerical techniques that belong to the class of structure-preserving finite Volume methods. Unstructured grids allow on the one hand a uniform coverage of the sphere without resolution clustering, and on the other hand they provide the freedom to intentionally cluster grid points in some region of interest. In this work we run **ICON-O** on a uniform grid of approximately 10 km resolution and on a grid with four times less degrees of freedom that is stretched such that in the resulting telescoping grid within the North Atlantic the two resolutions are similar, while outside the focal area the grid approaches smoothly ~ 80 km resolution. By comparison with observations and reanalysis data we show first, that the simulation on the uniform 10 km grid provides a decent mesoscale eddy rich simulation and second, that the telescoping grid is able to reproduce the mesoscale rich circulation locally in the North Atlantic and on decadal time scales. This telescoping technique of unstructured grids opens new research directions.

1. Introduction

The Max Planck Institute for Meteorology (MPI-M) has a long tradition in developing global ocean models (Maier-Reimer et al., 1993; Marsland et al., 2003; Wolff et al., 1997). The ocean general circulation model **ICON-O** continues this tradition. **ICON-O** constitutes the ocean and sea ice component of MPI-M's Earth system model **ICON-ESM**, described in Jungclaus et al. (2022), and schematically illustrated in Figure 1. The name “**ICON**” (**Icosahedral Nonhydrostatic Weather and Climate Model**) denotes a modeling framework and a weather and climate modeling system that is jointly developed by MPI-M, the German Weather Service (DWD), the German Climate Computing Center (DKRZ), and the Karlsruhe Institute of Technology. The **ICON** modeling system addresses seamlessly modeling for climate research as well as for numerical weather prediction. **ICON**'s ocean component **ICON-O** was developed at MPI-M. This paper provides a scientific documentation of **ICON-O** in uncoupled mode through an analysis of the simulated global ocean circulation. We demonstrate the model's

© 2022 The Authors. *Journal of Advances in Modeling Earth Systems* published by Wiley Periodicals LLC on behalf of American Geophysical Union. This is an open access article under the terms of the [Creative Commons Attribution-NonCommercial-NoDerivs License](https://creativecommons.org/licenses/by-nc-nd/4.0/), which permits use and distribution in any medium, provided the original work is properly cited, the use is non-commercial and no modifications or adaptations are made.

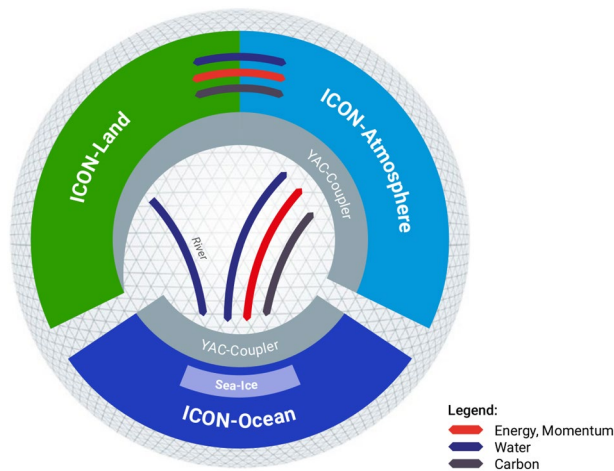


Figure 1. Schematic overview of the Icosahedral Nonhydrostatic Weather and Climate Model modeling system and its individual components.

capabilities in comprehensive ocean experiments and provide a thorough analysis of the simulated circulation on grids of uniform and of locally varying resolution.

The atmosphere model ICON-A (Crüger et al., 2018; Giorgetta et al., 2018; Zängl et al., 2015) and the ocean model ICON-O have been developed jointly. A main accomplishment of the joint development is that the two models share the same technical infrastructure that covers in particular High-Performance-Computing aspects. The requirements such a model infrastructure has to satisfy are complex. It has to make the model development efficient by implementing common features only once and, at the same time, it needs to be flexible enough to allow for differences wherever they are necessary. ICON's atmosphere and its ocean model differ for example, in the underlying dynamical equations and also in some numerical aspects, nevertheless both use the same data types on which the joint model infrastructure is built. The infrastructure also has to take into account different applications on a wide range of spatio-temporal scales from paleo-climate applications to ultra-high storm- and eddy-resolving resolutions.

The ocean component ICON-O operates—as do all ICON components—on a horizontal grid consisting of triangular cells and a vertically structured grid, given for example, by a z or a z^* -coordinate (Adcroft & Campin, 2004). The horizontal grid is described by generic data structures suitable for unstructured grids. A grid is defined to be unstructured if its connectivity cannot be written as an integer-array. Our data structures rely on the connectivity and neighborhood relations of the unstructured grid, but they are also applicable to structured grids. The grids that we use in this work are icosahedral grids, constructed by recursive subdivision of the icosahedron. Icosahedral grids belong to the class of structured grids (see e.g., Stuhne and Peltier (2009)) but they are treated in ICON as an unstructured grid. Icosahedral grids have become popular in ocean as well as in atmospheric modeling (Heikes & Randall, 1995a; Ringler et al., 2013; Stuhne & Peltier, 2006; Tomita et al., 2001). The fundamental difference between icosahedral and latitude-longitude grids is that icosahedral grids allow for a nearly uniform tessellation of the sphere. The grids uniformity is considered computationally advantageous, albeit the dynamics of the global ocean favor a nonuniform grid resolution that follows the Rossby radius and increases toward the poles.

This motivates the two questions that we address in this work. The first one is, if ICON-O with a uniform grid configuration able to simulate a ocean circulation that compares well with observations. The quality of the ocean circulation simulated by ICON-O has implications on ICON-ESM that relies on uniform grids as well. That unstructured grid ocean models are able to simulate the global ocean circulation has already been demonstrated (Ringler et al., 2013; Scholz et al., 2019, 2022). The question on the quality of the simulated circulation is first and foremost a question to the numerics of the model. The three existing global unstructured grid ocean circulation models, FESOM, MPAS-O, and ICON-O differ in terms of horizontal grid and variable staggering (FESOM uses a triangular grid and a quasi-B staggering, MPAS-O a hexagonal grid with C-type staggering and ICON-O employs a triangular grid with C-staggering). Therefore the discrete approximation spaces that these models use to solve the hydrostatic Boussinesq equations are different, and consequently the respective numerics also differ. A detailed description of the numerics underlying ICON-O is not given here but can be found in Korn (2017).

The second question we pursue is also related to the icosahedral grid and has its origin in the capability of unstructured grids to deviate from its originally uniform resolution and to locally increase the resolution by means of grid refinement. This refinement allows to study the circulation within a region of interest in more detail and with higher accuracy than outside this region. In this work we use a non-uniform grid that has four times less degrees of freedom than the considered uniform high resolution grid (see Figure 2). The non-uniform grid has a circular-shaped region in the North Atlantic where its resolution is similar to the uniform grid, while it coarsens smoothly with increasing distance from the North Atlantic. We refer to this model configuration as “telescoping” to emphasize that we are primarily interested in the dynamics within the focal region. The circulation outside this region is only relevant insofar as it provides a kind of “boundary condition” for the focal region. This model configuration avoids the special treatment of boundaries as in regional ocean models, which can become quite complex when the exchange between the regional domain and the rest of the ocean becomes dynamically relevant.

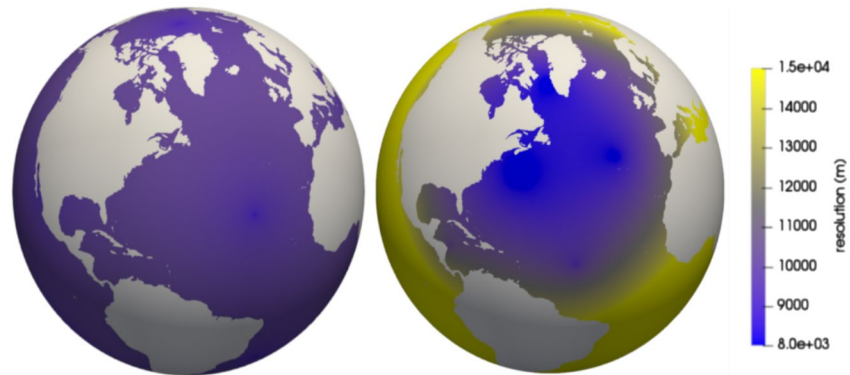


Figure 2. Illustration of the two experiments considered in this paper. The uniform configuration **ICON-O_{UG}** (left) and the telescoping configuration **ICON-O_{tele}** (right). Shown is the resolution, measured as square root of the product of primal and dual edge length. The configuration **ICON-O_{tele}** has globally four times less degrees of freedom than **ICON-O_{UG}** but a comparable number of degrees of freedom in the North Atlantic.

The choice of a circular-shaped focal region is no restriction. The flexibility in the specification of the refined area of interest and the associated zooming capability is one of the strengths of unstructured grid models. Examples of the flexibility in resolution changes within the grid with the unstructured grid ocean models FESOM and MPAS-O comprise Sein et al. (2019), where the horizontal resolution of FESOM aims to capture the variability of the sea surface height (SSH), in Hoch et al. (2020) the global grid of MPAS-O is refined toward the North-American coast, and Veneziani et al. (2022) refines the global MPAS-O grid in the Arctic Ocean. The works of Hoch et al. (2020) and of Logemann et al. (2021); Mathis et al. (2022) with MPAS-O and ICON-O respectively blur the lines between global and coastal ocean models by refining along the coast with a global model. In contrast, structured grid ocean models operating on latitude-longitude grids, can also implement a computational telescope by placing the grid poles over land (see e.g., Mikolajewicz et al. (2005); Marsland et al. (2004)) or by nesting (see e.g., Madec et al. (2016)). Placing the poles over land retains the orthogonality of the grid but allows less flexibility regarding placement and shape of the focal region, while nesting requires to handle open boundaries. Unstructured grid models can of course also operate as a limited-area model with open boundaries, as it was done with FESOM-C (Androssov et al., 2019). A nested configuration, as implemented for the ICON atmosphere model (Maurer et al., 2022), is currently not available for ICON-O.

We emphasize that our aim with the telescoping configuration of ICON-O is not to optimally distribute the given number of degrees of freedom to improve the global circulation, for example, via a resolution function that follows the deformation radius, as suggested in Hallberg (2013) and implemented in Sein et al. (2019). Instead we assume that a scientific question singles out a specific region and we use the North Atlantic as an example. The highly resolved focal region can be positioned freely at any point in the world ocean, based solely on the interests of the modeler. Regarding the notion, we have invoked the metaphor of a computational telescope, because the term “grid refinement” does not convey the same meaning as “telescoping.” The term grid refinement may also raise associations with adaptive grid refinement, which is not considered here, all refinements are static.

The two abilities, first, to simulate global ocean dynamics on a uniform grid and second, to employ a variety of nonuniform grids, constitute in our opinion the core requirements for any ocean model using an unstructured grid. To demonstrate that ICON-O satisfies the above mentioned core requirements of unstructured grid global ocean models, we carry out two experiments: the first one at a global and nearly uniform resolution of ~ 10 km (the definition of the “resolution” is given in Section 2.1.1), and a second, telescoping one, that modifies a 20 km-grid by shifting grid nodes such that a highly resolved focal area with a maximal resolution of ~ 8 to 9 km in the North Atlantic is created. These two model configurations are denoted **ICON-O_{UG}** and **ICON-O_{tele}**, respectively. In the second experiment the resolution coarsens smoothly with increasing distance to the North Atlantic and reaches a minimal resolution of ~ 80 km near Australia (see Figure 3). For **ICON-O_{tele}** we have chosen a smooth resolution change but steeper resolution gradients that offer bigger computational savings might be possible. At 10 km grid spacing the model allows for a good representation of mesoscale eddies in low and mid latitudes, but not at higher latitudes. We therefore call the **ICON-O_{UG}** grid “eddy-rich,” rather than “eddy-resolving.”

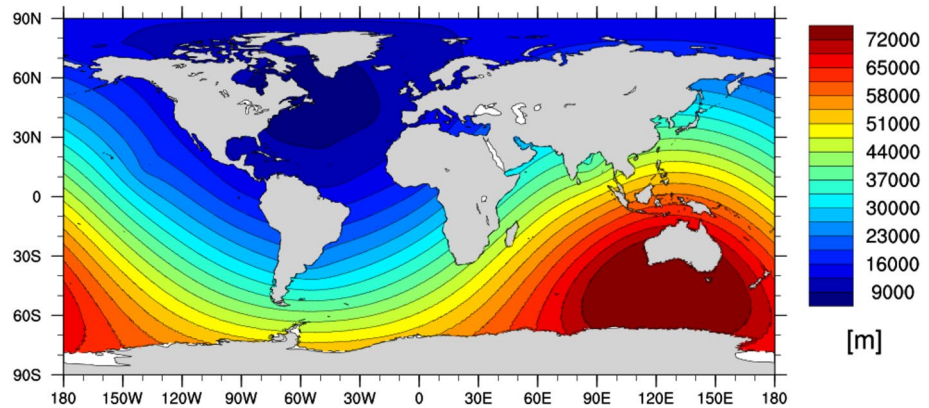


Figure 3. Resolution variation of the refined configuration $\text{ICON-O}_{\text{tele}}$.

The analysis of our numerical experiment with $\text{ICON-O}_{\text{UG}}$ compares the simulated global circulation to a climatological mean state as well as to observations. Then we use the uniform simulation as a reference and compare it with the locally refined configuration in the North Atlantic, where both configurations have a similar resolution. It is of great practical and theoretical relevance to know if and how the model is able to approximate the circulation locally in space and time. The comparison between uniform and telescoping model configuration $\text{ICON-O}_{\text{UG}}$ and $\text{ICON-O}_{\text{tele}}$ focuses on the dynamical core with a minimal set of subgrid scale closures. We deliberately do not address the problem of scale-aware parametrizations, this topic is beyond the scope of the current paper.

In Section 2, we describe the main characteristics of the model. We continue in Section 4 with the experimental configuration on the uniform and on the locally refined grid. Section 5 describes the computational performance of the model. The paper ends with a discussion and conclusion in Section 6.

2. Model Description

ICON-O solves the hydrostatic Boussinesq equations of large-scale ocean dynamics with a free surface, also referred to as the primitive equations of large-scale ocean dynamics. The ocean primitive equations are an evolution equation for a state vector $\{v, \eta, \theta, S\}$ that consists of a horizontal velocity field v , the surface elevation η and the oceanic tracers, potential temperature and salinity $\{\theta, S\}$. A comprehensive description of the numerical concept underlying ICON-O can be found in Korn (2017). Below we sketch the model's key components. Since model development is an ongoing dynamical process we mention also briefly actual developments that will be available soon in future applications.

2.1. Spatial and Temporal Discretization

The description of ICON-O's spatio-temporal discretization starts with the discretization of the model domain. We introduce the grid first, before we continue with the variable staggering, the discrete differential operators and the reconstructions.

2.1.1. Model Grid—Uniform and Refined Resolution

2.1.1.1. Model Grid—Uniform Configuration

The horizontal grid is composed of triangular cells, identified with their circumcenter. It is generated through a subdivision of the icosahedron that is inscribed into a sphere. The 12 vertices of the icosahedron are located at the North and South Pole, and uniformly distributed at 26.565°N and 26.565°S . The icosahedron consists of 30 edges and 20 cell centers. The subdivision bisects the edges and uses the edge midpoints as vertices of the next refinement levels. This results in a quad-tree structure. The subdivided triangles are then projected onto the surface of the sphere. An overview of using icosahedral grids can be found in Satoh (2013). Connecting the triangular cell centers around a vertex creates the so-called *dual grid*. The projection onto the sphere damages the perfect regularity of the original icosahedron. It leads to relatively small deviations of the edge length and the distance between cell circumcenters. These deviations decrease with increasing refinement levels of the icosahedron,

that is, with increasing resolution. Another consequence is that the dual grid does no longer consists solely of hexagons—as it is the case for the original icosahedron—but comprises also 20 pentagons.

For the uniform grids used in this paper this construction is modified by reflecting the Northern Hemisphere to the south. This creates an additional equatorial symmetry that the original grid does not satisfy. The same result can be achieved by twisting the icosahedron as in Heikes and Randall (1995a, 1995b). The symmetrized grid has been tested with ICON-O in shallow water set-ups and showed a reduction of the truncation error (Korn & Linardakis, 2018). The ICON grid generator is capable of different refinement options such as trisecting edges, but this option is not pursued here. To this basic grid generation a *grid optimization* procedure is applied in ICON's grid generator that minimizes the trade-off between variations of the triangular edge length and the distance between cell centers. The model's infrastructure allows to use a variety of triangular grids that need not necessarily be derived from the icosahedron. An example of a non-icosahedral grid with a resolution that increases toward the poles, analogous to latitude-longitude grids, can be found in Korn and Linardakis (2018).

For the definition of the nominal grid resolution we follow the convention used in the ICON modeling system (Crüger et al., 2018; Giorgetta et al., 2018; Wan et al., 2013; Zängl et al., 2015) and define the nominal grid resolution as the square root of the product of edge length and cell center distance. For the **ICON-O_{UG}** grid this quantity varies slightly (between 8.4 and 10 km).

The vertical grid is structured and non-uniform (referred to as z coordinate). The two-dimensional triangles and hexagons/pentagons are simply extended by a height-based dimension such that three-dimensional prisms are generated. The number of vertical coordinate levels is fixed, but the number of vertical levels with cell centers inside the ocean domain depends on the topography and varies from column to column. The thickness of the prisms is constant in time, except for the surface layer, where the sea surface elevation evolves according to the free surface equation and where the sea ice is taken into account (for details we refer to Korn (2017)). The choice of the most appropriate vertical coordinate system for ocean general circulation models is subject of ongoing research (see e.g., S. M. Griffies et al. (2020)). In this direction Arbitrary-Lagrangian-Eulerian coordinates have been developed (see e.g., Adcroft et al. (2019)) that allow the use of different vertical coordinates in different regions of the world ocean. In the work presented here, we use the classical z -coordinates with its well-understood advantages and disadvantages. Alternative vertical coordinates are implemented in an Eulerian fashion in ICON-O and are described in Korn et al. (2022). A full Arbitrary-Lagrangian-Eulerian treatment of the vertical coordinate is currently not implemented in ICON-O.

2.1.1.2. Model Grid With Local Refinement

We apply the technique of *spring dynamics* as described in Tomita et al. (2001, 2002) to transform the uniform to a nonuniform grid and with higher resolution in a specified target region. Spring dynamics describes the grid vertices as connected by springs with a certain elasticity that allows changing their position. Spring dynamics implements a smooth transition from the higher to the lower resolutions, maintaining a grid quality similar to the icosahedral grid. The maximum angle between the edges of a triangle in the modified grid for example, is 74° . Other, more powerful and sophisticated approaches may also be used, like Engwirda (2017), but while they provide sharper control of the refined areas, the maximum angle is slightly larger (78°). As shown in Logemann et al. (2021), the model is able to run on grids with larger angles, so more powerful grid generator methods can be used in the future. A consequence of the refinement technique via spring dynamics is that a coarsely resolved region is created on the opposite side of the globe (see Figure 3). A different strategy with refinement along coastlines is described in Logemann et al. (2021) and Mathis et al. (2022).

2.1.2. Discrete Variables and Their Operators

The spatial discretization of ICON-O uses a mimetic discretization of the differential operators. This discretization methodology mimics on the discrete level important relations from continuous vector calculus (see e.g., da Veiga et al., 2014; Lipnikov et al., 2014). The novelty of the ICON-O numerics is a new use of reconstructions that are required to combine scalar and velocity fields for the calculation of fluxes. For these reconstructions we introduced the concept of *Hilbert-space compatible reconstructions* (Korn, 2017; Korn & Linardakis, 2018). These reconstructions have the important property to be compatible with a discrete scalar product for the state space of the ocean model consisting of velocity, temperature and salinity. This property allows us to write the discrete primitive equations in a discrete weak/variational form. A discrete weak form is a necessary condition to derive discrete global conservation principles. The design of ICON-O has been centered around discrete

conservation principles. A second and equally important advantage of Hilbert-space compatible reconstructions is that for the triangular grid with a Arakawa C-type staggering they allow to control a spurious mode in the divergence field (see e.g., Danilov, 2010; Wolfram & Fringer 2013) through a projection operator. This projection is compatible with the conservation laws and preserves for example, energetic consistency. For details we refer to Korn (2017) and Korn and Linardakis (2018).

2.1.2.1. Variable Staggering

On the triangular grid introduced in Section 2.1.1 we define an Arakawa C-type staggering of variables. The scalar variables such as temperature are defined as constant functions within a triangular cell. These functions can be identified with point values at the cell circumcenter. The velocity description uses only the normal component of the velocity vector, this normal component is described as a piecewise constant function on triangular edges and can be identified with a point value at the edge midpoint. The same staggering is used in MPAS-O (Ringler et al., 2013) with the difference that the role of the primal/dual grid are exchanged. The vertical component of vorticity appears in our model equations as a consequence of the vector invariant form of the velocity equation. This scalar quantity is associated with triangular vertices and assumed to be constant on dual grid cells. All of these discrete quantities are defined on the middle level of the three-dimensional triangular or hexagonal prisms. The vertical velocity is a piecewise constant scalar function at the top/bottom of the triangular prisms.

2.1.2.2. Differential Operators

On the model grid and based on the C-type staggering we define coordinate-invariant discrete differential operators of divergence and curl by discrete versions of the integral theorems of Gauss and Stokes. Both operators are defined in terms of fluxes on the primal and the dual grid respectively and map these fluxes to the vector space of functions that are constant on primal and dual cells, respectively. Following the idea of *mimetic finite difference* discretizations (see e.g., Lipnikov et al., 2014) the derivatives in normal and tangential directions are defined as transposed operators to divergence and curl with respect to a scalar product on the respective discrete Hilbert space. These properties are essential in deriving energetic consistency (for details we refer to Korn (2017)).

2.1.2.3. Hilbert Space Compatible Reconstructions

The variable staggering places scalar and velocity variables at different locations and consequentially these variables are elements of different discrete spaces. The product of scalar and velocity variables is needed to calculate fluxes of volume, temperature or vorticity. This problem is solved in a structure-preserving way that is compatible with the discrete conservation laws by means of the new concept of *Hilbert space compatible reconstructions*. This class of reconstructions respect the discrete scalar products of the vector spaces of scalar and vector variables and are compatible with the domain and image of the discrete differential operators. Hilbert Space Compatible Reconstructions imply a non-dissipative filter in the discrete continuity equation. This filter is the key to control the divergence mode of the triangular C-grid, mentioned above. Hilbert space compatible reconstructions are the distinguishing feature of ICON-O. For details we refer to Korn (2017).

2.1.2.4. Tracer Transport

The tracer advection uses a flux-corrected transport algorithm consisting of an upwind scheme as the low-order transport component and a higher-order transport scheme that relies in the horizontal direction on Hilbert space compatible reconstructions and vertically on a piecewise-parabolic reconstruction (Colella & Woodward, 1984). For horizontal as well as for vertical transport the relative weight of low- and high-order schemes in the flux-corrected transport algorithm is determined by a Zalesak limiter (Zalesak, 1979). For details we refer to Korn (2017).

2.1.2.5. Time Stepping

The time stepping is a classical semi-implicit Adams-Bashford-2 scheme. The fast dynamics of the free surface equation is integrated implicitly by solving a two-dimensional elliptic equation in each time step. This alleviates severe time step restrictions due to the fast dynamics. ICON-O allows for a nonlinear evolution of the free surface, where the thickness of each water column varies in time and where freshwater fluxes due to precipitation/evaporation and river runoff are directly applied (for a discussion between the differences of a linear vs. a nonlinear free surface we refer to Scholz et al. (2019)). Once the free surface equation is solved the velocity and tracer variables are moved forward in time with an Adams-Bashford extrapolation. The linear elliptic free surface equation is

solved iteratively with a conjugated gradient method. As a consequence of the consistency between the surface equation and the discrete continuity equation are the Hilbert Space Compatible Reconstructions and the resulting projection part of the elliptic free surface equations. It is worth mentioning that the presence of these operators in the equation for the free surface improves the condition number of the matrix in the free surface equation and leads to faster convergence. The details are given in Korn (2017).

2.2. Parametrizations

2.2.1. Velocity Dissipation

In ocean general circulation models, velocity dissipation (or friction) is parametrized by practical considerations rather than first principles. The guiding principle for horizontal friction is to use minimal viscosity for stability reasons while controlling grid-scale noise and resolving western boundary currents. Since no coherent theory exists that guides the choice of the dissipation scheme, ICON-O comprises a range of options to implement dissipation. This includes a “harmonic” Laplace or a “biharmonic” operator by iterating the Laplacian. The viscosity parameter can be determined as a constant value or scaled in terms of geometric grid quantities such as the edge length of the triangular area, or it can be determined in a flow-dependent fashion following the modified Leith closure, in which the eddy viscosity is determined from the modulus of vorticity alone or together with the modulus of divergence (see e.g., Fox-Kemper & Menemenlis, 2008).

In the numerical experiments shown here we employ for horizontal friction the biharmonic dissipation operator D_v , defined by

$$D_v : = K^v \Delta_v^2 v, \quad (1)$$

with the vector Laplacian $\Delta_v v := \nabla \operatorname{div}(v) - \operatorname{curl}^T \operatorname{curl}(v)$,

and with horizontal viscosity $K^v = K_{ref} \sqrt{|e| |e^\perp|}$

where v denotes the normal edge velocity, $|e|$ $|e^\perp|$ the edge length and the cell center distance, respectively and $K_{ref} > 0$ is a fixed reference viscosity. The vertical friction A_v uses the Laplace operator in each vertical column

$$A_v v = D_z (A^v D_z v), \quad (2)$$

where the vertical derivatives D_z , D_z act on full and half levels respectively. The calculation of the vertical viscosity A^v is described in Section 2.2.2 as part of the vertical mixing scheme.

2.2.2. Vertical Mixing

The parametrization of turbulent vertical mixing in ICON-O relies on a prognostic equation for turbulent kinetic energy (TKE) and implements the closure suggested by Gaspar et al. (1990), Blanke and Delecluse (1993), and Eden et al. (2014). Here, a mixing length approach with the generic Ansatz for the vertical mixing coefficient for velocity and oceanic tracers $A^{v,C} = c_{v,C} \mathcal{E}^{1/2} L_{mix}$ is used, where \mathcal{E} denotes the TKE, L_{mix} the mixing length and $c_{v,C}$ a dimensionless adjustable constant. The TKE \mathcal{E} evolves according to the vertical (one-dimensional) TKE equation

$$\partial_t \mathcal{E} = \partial_z (\alpha_{TKE} A^v \partial_z \mathcal{E}) - A^C N^2 + A^v (\partial_z v)^2 + D_{sw} - D_{heat}, \quad (3)$$

where N^2 denotes the buoyancy frequency, D_{sw} , D_{heat} the dissipation due to surface wave breaking and conversion of TKE into heat. Equation 3 describes the evolution of TKE due to the terms on the right-hand side. The first term on the right-hand side describes the vertical diffusion of TKE. The second term represents the exchange of TKE with mean potential energy such that TKE is increased in case of unstable stratification and convective mixing, and decreased in case of stable stratification. The third term implements the exchange of TKE with mean kinetic energy by vertical shear production of the velocity field. The TKE Equation 3 is supplemented either by the Dirichlet boundary condition

$$\mathcal{E} = \max(E_{tke,min}, c_d |\tau / \rho_0|) \quad \text{at } z = 0, \quad (4)$$

or by the Neumann boundary condition

$$\alpha_{TKE} A^v \partial_z \mathcal{E} = c_d \left| \frac{\tau}{\rho_0} \right|^{3/2} \quad \text{at } z = 0, \quad (5)$$

where τ denotes the wind stress and c_d a tuning coefficient. From \mathcal{E} , the vertical viscosity A_v and diapycnal diffusivity A^C are derived as:

$$A^v = c_u \mathcal{E}^{1/2} L_{\text{mix}}, \quad \text{and} \quad A^C = c_b \mathcal{E}^{1/2} L_{\text{mix}}, \quad (6)$$

where c_u, c_b are constants. The simple parametrization $L_{\text{mix}} = \sqrt{2\mathcal{E}/N^2}$ for the mixing length L_{mix} is used (Blanke & Delecluse, 1993). The vertical variation of this length scale is bounded $|\partial_z L_{\text{mix}}| < 1$ which also ensures that L_{mix} is bounded by the vertical distances between this point and the surface or the bottom. In the interior ocean and sufficiently far away from the boundary, where vertical mixing is mainly caused by breaking of internal waves, TKE is set to a constant background value of $TKE_{\text{min}} = 10^{-6} \text{ m}^2/\text{s}^2$. More sophisticated parameterizations for interior mixing, where an additional equation for internal waves is applied following D. Olbers and Eden (2013), are also available but are not used in the simulations of this paper.

In addition to the TKE-scheme used here, ICON-O comprises options for vertical mixing via the K-profile parametrization (KPP; W. Large et al., 1997; W. G. Large et al., 1994) and a modified Pacanowsky-Philander-scheme that incorporates additional wind mixing (Marsland et al., 2003; Pacanowsky & Philander, 1981).

2.2.3. Eddy Induced Diffusion and Eddy Induced Advection

The stirring and diffusion that mesoscale eddies exert on oceanic tracers are parametrized at coarse resolution in general ocean circulation models. ICON-O parametrizes the eddy-induced diffusion and advection following Redi (1982) and Gent and McWilliams (1990), respectively. ICON-O employs the classical variational approach (S. Griffies, 1998; S. Griffies et al., 1998) but discretizes the variational functional by inherently unstructured grid methods and not by the classical triad-approach that was developed originally for structured grids. Hilbert-space-compatible reconstructions and mimetic differential operators of ICON-O's dynamical core allow a structure-preserving discretization of the eddy parametrization. Full details are given in Korn (2018). Parameter values of the mesoscale eddy parametrization can be chosen to be constant or to vary with depth following the closure of Danabasoglu and Marshall (2007).

2.3. Sea Ice Model

The sea ice model consists of a dynamic and a thermodynamic component. Thermodynamics describes the freezing and melting of sea ice by a single-category, zero-layer formulation (Semtner, 1976) (see Appendix A). The current sea ice dynamics is based on the sea ice dynamics component of FESIM (Danilov et al., 2015). It solves the momentum equation for sea ice with an elastic-viscous-plastic (EVP) rheology, following the formulation by Bouillon et al. (2013). However, because ICON-O is based on a C-grid while FESIM is based on the analog of an A-grid staggering, a wrapper is needed to transfer variables between the ICON-O grid and the sea ice dynamics component. The details of this wrapper are described in Appendix A). The approach of modeling sea ice and ocean dynamics on different staggarings creates inevitable artifacts. For this reason a new sea ice model is currently being developed that operates on ICON's native triangular C-grid. The numerical approach to discretize the stress tensor on this grid is described in Mehlmann and Korn (2021). A comparison of the new dynamics with other approaches was made by Mehlmann et al. (2021). This new sea ice dynamics will replace the configuration described here, and results of the new ocean-sea-ice configuration of ICON-O will be reported elsewhere.

2.4. Equation of State

The thermodynamics concept used in ICON-O is currently based on the thermodynamics variables potential temperature and practical salinity. In this work we have used the UNESCO equation of state (UNESCO, 1981). Alternative equations of state such as the one by Jackett et al. (2006) are available but have not been considered in this work. The more accurate and theoretical consistent thermodynamic description in terms of conservative temperature and absolute salinity, described in the standard TEOS-10 (UNESCO, 2010), with its associated equation of state is under consideration.

2.5. Model Development, Software Construction, and Code Verification

For the ocean primitive equations no exact solutions are known that can be used as a benchmark against which ICON-O could be tested to verify the correctness of the code. We accommodated for this difficulty through our model and our software development strategy. Regarding the model development, ICON-O (as well as ICON-A) were developed in layers by separating first, the dynamical core from the parametrizations and second, within the dynamical core the horizontal from the vertical dynamics. Each of these layers was then further subdivided into smaller elements such as the divergence operator or the vertical Laplacian. The smallest elements were subject to unit tests to test the correctness of the code. We then aggregated the smallest elements and tested the horizontal dynamics in the context of the shallow-water equations. Here, the new components of our numerical scheme such as the Hilbert-Space compatible reconstructions were of particular importance. The results of these tests were reported in a series of publications: in Korn and Danilov (2017) the wave propagation properties of the mimetic discretization and the Hilbert-Space compatible reconstructions were investigated, Korn and Linardakis (2018) studied the horizontal discretizations in the framework of the shallow-water equations with a focus on conservation properties. This paper also contains accuracy results on the differential operators. The new discretization of the eddy-parametrization was introduced in Korn (2018) with idealized tests for the eddy-advection operator and the eddy-diffusion operator, as well as through a coarse-resolution global ocean simulation. The paper by Korn (2017) formulates the numerical basis of ICON-O. The paper contains a series of tests, from idealized tests such as the Munk Gyre to a global ocean simulation at eddy-permitting resolution. The vertical mixing schemes that are available for ICON-O, the TKE, KPP, and PP-schemes have been tested in MPI-OM (Gutjahr et al., 2021) and the code for vertical mixing was then integrated into ICON-O. All of this prior work contributed to the confidence of ICON-O's code and can be seen as a prelude to the current paper.

Our model development strategy was reflected by our accompanying software development strategy. ICON-O is written in FORTRAN90 and uses the object-oriented software development philosophy. User defined data types were constructed that map algorithmic components such as the grid or the state vector onto data types (objects) and these objects are passed through the algorithm. This leads to a natural encapsulation of the model data and it also facilitates the construction of the overall model algorithm as a series of building blocks that communicate through defined interfaces. ICON-O's infrastructure contains a "testbench" that enables us to isolate individual code elements such as differential operators or mixing schemes and test them separately from the complete model while at the same time remaining within the technical infrastructure of the model such that, for example, parallelization and I/O are available.

The code of ICON-O is part of the ICON source code repository and version control system that contains the code of all ICON-models. With the repository comes a dedicated development cycle that consists of the steps, development, unit tests and integration into the actual model version once gatekeeping tests are passed. Additional technical tests check that the model compiles on different platforms. These measures allow us to parallelize the development process among distributed developers, hosted at different institutions and preserve the integrity of the model code.

3. Model Configuration

Our experimental set-up aligns with requirements of the envisioned application of ICON-O as part of a prediction system for seasonal to decadal time scales at mesoscale-eddy resolving resolution. For this purpose it is important to ensure that the ocean model is able to create a realistic eddy field that is then part of the initial conditions for a prediction. To foreshadow the use of ICON-O as part of a prediction system, we force the model with the transient high-resolution and high-frequency reanalysis from NCEP and ERA5. The use of the two forcing data sets enables a robust assessment of model responses (see Section 3.2). Due to the computational costs we have to restrict the integration times to a few decades.

For the uniform simulation **ICON-O_{UG}** we use a horizontal grid with a nearly uniform resolution of ~ 10 km (cf., Section 2.1.1). The grid has 128 vertical levels, with a spacing that ranges from 8 m in the upper ocean to 200 m toward the bottom. The top layer has a thickness of 11 m to avoid stability problems that potentially arise from large surface elevation changes. For the bathymetry we use for both configurations the SRTM30 data set (Becker et al., 2009), which has a resolution of ~ 900 m. The bathymetry data is interpolated to the model grid by a nearest neighbor interpolation. Manual quality control ensures that the width and depth of important channels such as

Denmark Strait or the Strait of Gibraltar are not affected by interpolation errors. Then the land-sea mask of the first level is used to remove all dry grid points throughout the whole water column. This reduces the total number of used grid points considerably, improves the computational efficiency and reduces memory requirements. If we would apply the land-sea mask individually to all layers to remove all land points, this would require indirect addressing in the vertical direction, while leading only to a small additional reduction of the grid points. The additional gain was considered not big enough to outweigh the code complexity.

3.1. Telescoping Configuration

For the telescoping configuration **ICON-O_{tele}** a base grid of ~ 20 km resolution with four times less grid cells as the grid of the **ICON-O_{UG}** configuration was modified by spring dynamics (cf., Section 2.1.1) to obtain the resolution change shown in Figure 3. The resulting focal area has a resolution that is similar but slightly higher (~ 8 to 9 km) than for the uniform grid. As a consequence of the refinement technique by spring dynamics the strongest loss of resolution occurs in the Indo-Pacific. The resolution in the Southern Ocean varies between 50 and 80 km. The number of vertical levels and the vertical spacing of **ICON-O_{tele}** is identical to the uniform configuration **ICON-O_{UG}**.

3.2. Initial Conditions, Surface Forcing, and Spin-Up

To generate an initial state a climatological distribution for temperature and salinity from the Polar Science Center Hydrographic Climatology (PHC3; Steele et al., 2001) is interpolated to the respective grid by means of a bilinear interpolation using the Climate Data Operators (Schulzweida, 2021). The spin-up follows the procedure of the STORM experiment (von Storch et al., 2012). For 25 years a 1-year periodic forcing with a daily frequency using the climatological data set (Röske, 2006) was applied. After the 25-years spinup the models kinetic energy has reached a quasi-steady state (not shown). We apply now from 1948 to 2019 the transient and daily forcing from the NCEP data set (Kalnay et al., 1996) that has a spatial resolution of 200 km. In the year 1980 we branch off and apply from 1980 to 2019 the ERA5 forcing (Hersbach et al., 2018). The ERA5 forcing has a spatial resolution of ~ 30 km and temporal frequency of 1 hr. We remark that the grid of **ICON-O_{tele}** has in some regions a coarser resolution than the atmospheric forcing, such that **ICON-O_{tele}** effectively sees there an averaged atmospheric forcing.

The atmospheric forcing data sets do not contain all necessary fluxes to prescribe the oceans boundary condition. They contain shortwave/longwave heat fluxes but the turbulent fluxes are calculated by means of bulk formulas. More specifically, from the atmospheric reanalysis we read in downward shortwave radiation, precipitation, sea level pressure, 2 m temperature, dew point temperature, cloud cover, 10 m wind speed and wind stress, then we use the bulk formulae described in Marsland et al. (2003) to calculate evaporation, fluxes of latent and sensible heat. All data were interpolated to the model grid with CDO's bilinear interpolation (Schulzweida, 2021), except for the windstress that was interpolated with a bicubic interpolation. For salinity we apply in the surface layer a restoring to the salinity of the PHC3 data (PHC3, Steele et al., 2001) with a time scale of 3 months with respect to the 11 m thick surface layer. For the river runoff we use the daily climatology from (Röske, 2006) that uses the observed mean monthly discharge of the world's 50 largest rivers (Gates et al., 1993). The applied surface fluxes of volume by precipitation, evaporation and runoff change the sea level and the global ocean volume. This is a desirable feature for coupled models but in an uncoupled configuration the global volume flux from the forcing is not necessarily balanced, because parts of the fresh water fluxes are prescribed (precipitation and runoff) while others are calculated from the model state (evaporation). To avoid a drift of the global ocean volume in the uncoupled configuration the global mean sea level is normalized to zero once per day. A notable difference between the two forcing data sets is that NCEP has a downward shortwave radiation that is ~ 15 to 20 W/m^2 stronger than for ERA5. This results in a too warm sea surface temperature (SST) field. To prevent too much sea-ice melting, we have increased the albedo in the NCEP-forced run by 5%. Our analysis focuses on the ERA5 simulation, the results with the NCEP forcing are qualitatively similar, and our results appear to be robust with respect to the two forcing sets. For **ICON-O_{UG}** and **ICON-O_{tele}** exactly the same spin-up procedure and surface forcing is used to achieve comparability of the two configurations.

3.3. Parameter Choices

The simulation of the **ICON-O_{UG}**-configuration uses a time step of 300 s. The time step was chosen conservatively and could have been larger without causing stability issues. For horizontal viscosity we use the biharmonic operator (a) with the reference viscosity $K_{ref} = 2.0E10$ m/s (cf., (a)). This value is scaled with the cube of the local grid resolution. This is the only place where a parameter is adapted to the varying resolution. The eddy parametrization was disabled in both runs. The horizontal diffusivity in the temperature and salinity equation is also deactivated but a diffusive effect on temperature and salinity is due to the flux limiter in the transport term. The vertical viscosity and diffusivity are determined by the TKE scheme (see Section 2.2.2) with the following parameters: $c_u = 0.1$, $c_b = c_u/(6.6Ri)$, $c_d = 3.75$, $\alpha_{TKE} = 30.0$, $TKE_{min} = 10^{-6}$ m²/s², where Ri denotes the Richardson number. For TKE the boundary condition of Neumann type was used in our simulations (see Equation 5 in Section 2.2.2). This TKE configuration was used for **ICON-O_{UG}** as well as for **ICON-O_{tele}**. The resolution of **ICON-O_{UG}** resolves considerable parts of the mesoscale eddies in the region of interest, therefore the eddy parametrization has been deactivated.

4. Evaluation of the Simulated Global Circulation for Uniform and Telescoping Configuration

In this section we describe the circulation simulated by **ICON-O** in its two configurations. Key diagnostics such as temperature and salinity biases or volume transport are compared to observations or a climatology. Guiding questions of our analysis are: how close is **ICON-O_{UG}** to ocean observations and how close is **ICON-O_{tele}** to **ICON-O_{UG}**. The considered time period are the last 10 years (2010–2019) of the simulation driven by ERA5-forcing. Unless stated otherwise, we consider means over this period for our analysis. Coupled climate models are often evaluated using 30-year averages as this is considered the “climate scale” and to have time averages large-enough to reduce the influence of climate variability that could be different in the coupled model compared to reanalysis. Since we are using forcing from reanalysis we can assume that the model should be quite constrained to the imposed variability and that a 10-year average is appropriate.

4.1. Surface Climate

The SST and the sea surface salinity (SSS) are defined as potential temperature and salinity of the first model level. Figure 4 shows the respective time averaged difference of SST and SSS from the two model configurations **ICON-O_{UG}** and **ICON-O_{tele}** to the PHC climatology. The time averaging of the model results is applied over the period 2010–2019 and the reference PHC climatology is interpolated to the first model level. We refer to this difference as “bias.”

The SST bias and the SSS bias of **ICON-O_{UG}** appear to be very similar to the respective bias of **ICON-O_{tele}**. In particular in the Northern Hemisphere the biases differ only in small scale features. Both configurations show in the Northern Hemisphere a warm SST bias. Part of this warm SST bias might be due to the spin-up procedure in which we branched off with the ERA5-simulation from the NCEP run after 32 years (cf., Section 3). The warm SST bias of the NCEP run might be inherited by the ERA5-simulation. Stronger biases appear at the Gulf Stream, the Kuroshio, the Labrador Sea, and generally in coastal regions. Noticeable is the localized cold bias at the Northwest corner of the Gulf Stream that is apparent in the SST of **ICON-O_{UG}** and of **ICON-O_{tele}**. At the same position we observe a fresh bias in the SSS of both configurations. In the Southern Hemisphere both **ICON-O_{UG}** and **ICON-O_{tele}** show predominantly a cold bias over large parts of the equatorial Atlantic and Pacific that changes to a warm bias in the Southern Ocean. Noticeably is a different bias structure in the Agulhas region, where **ICON-O_{tele}** shows a pronounced and more coherent cold bias east of South Africa and a warm bias west of Africa, while **ICON-O_{UG}** has in these regions weaker biases of opposite sign. This difference is likely due to the absence of the Agulhas retroflection in **ICON-O_{tele}** due to insufficient resolution (cf., also the difference in eddy kinetic energy between **ICON-O_{UG}** and **ICON-O_{tele}** in Figure 16). The main difference in the SSS is the pronounced fresh bias of **ICON-O_{tele}** in the Pacific near Australia that is considerably weaker in **ICON-O_{UG}**. In this region the two model configurations have the largest difference in resolution. Apart from these differences the SSS bias is similar in both experiments. This is due to the fact that in both experiments the models surface salinity is restored to the PHC climatology.

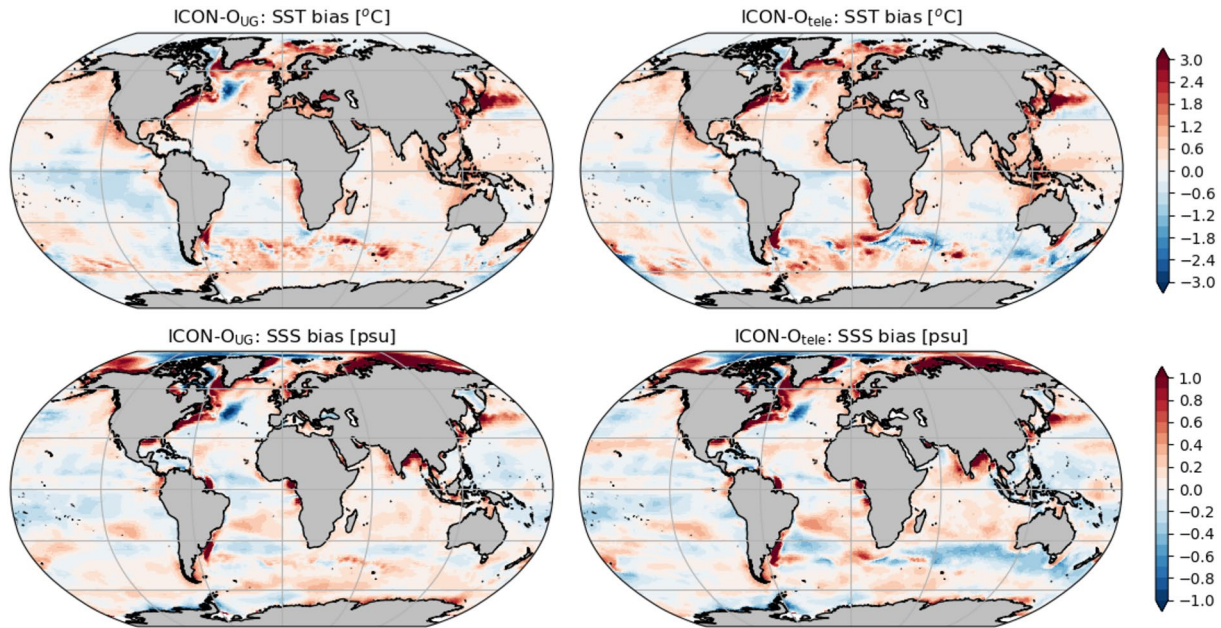


Figure 4. Maps of time averaged difference of surface temperature and salinity to Polar Science Center Hydrographic Climatology climatology at the first model level in 5.5 m depth. Left row shows the result for **ICON-O_{UG}**, the right row for **ICON-O_{tele}**.

4.2. Biases in Hydrography

Information about the structure of the simulated temperature and salinity fields in the ocean interior can be obtained from temporally and zonally averaged difference between the model results and the PHC climatology interpolated to the model grid. The averaging period are the years 2010–2019. This difference is again referred to as “bias.” In Figure 5 we observe for temperature a maximum bias of $\sim 2^{\circ}\text{C}$ at $\sim 60^{\circ}\text{N}$ that is present in **ICON-O_{UG}** as well as in **ICON-O_{tele}** but slightly weaker in the uniform configurations. Also the cold bias near

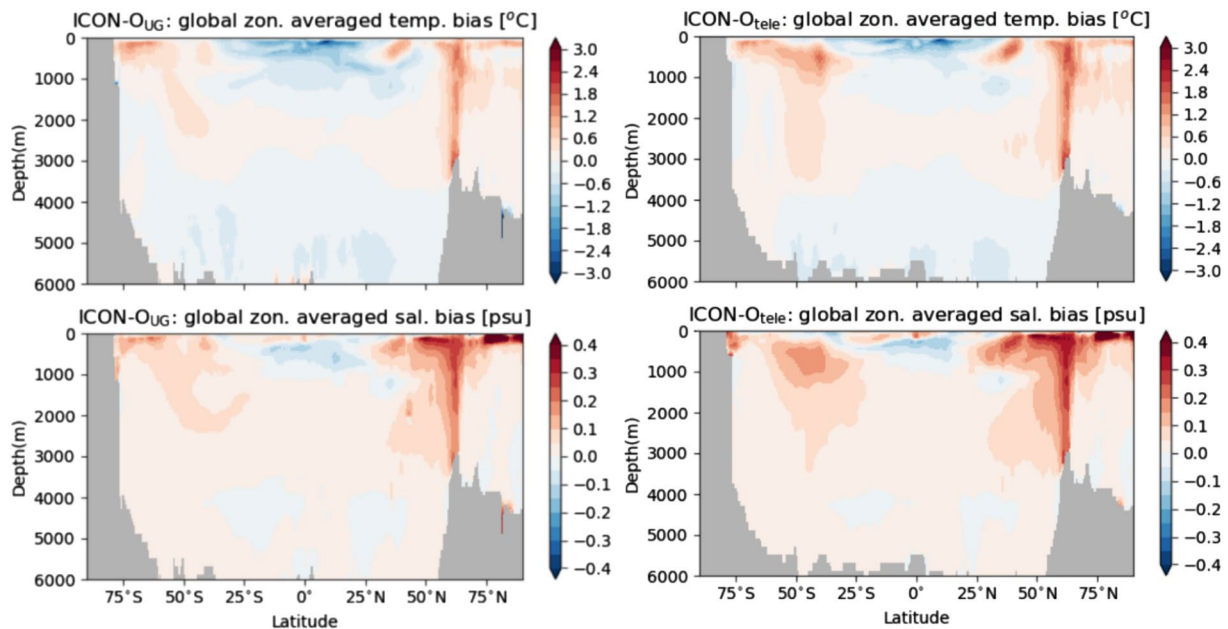


Figure 5. Global zonal average of bias relative to the Polar Science Center Hydrographic Climatology climatology for potential temperature (top) and salinity (bottom), **ICON-O_{UG}** is shown in the left column and **ICON-O_{tele}** in the right column.

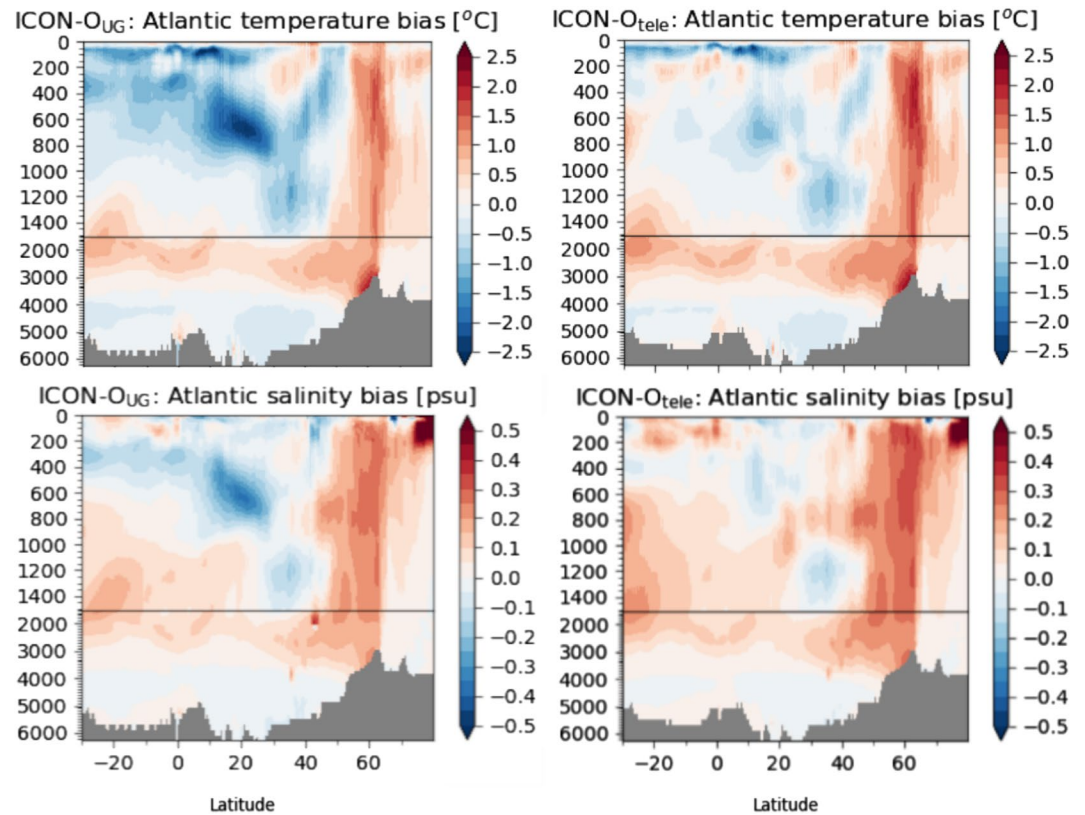


Figure 6. Atlantic: zonal average of bias relative to the Polar Science Center Hydrographic Climatology climatology for potential temperature (top) and salinity (bottom), $\text{ICON-O}_{\text{UG}}$ is shown in the left column and $\text{ICON-O}_{\text{tele}}$ in the right column.

the surface is similar in both configuration. In the Northern Hemisphere, the bias patterns and magnitudes of the two configurations are quite similar.

In the Southern Hemisphere, a warm temperature bias for $\text{ICON-O}_{\text{UG}}$ and $\text{ICON-O}_{\text{tele}}$ can be noted between $\sim 80^\circ$ to 30°S , it reaches from the surface down to $\sim 3,000$ to $3,500$ m. This bias is more pronounced in $\text{ICON-O}_{\text{tele}}$ (right) than in $\text{ICON-O}_{\text{UG}}$ (left). Qualitatively analogous statements apply to the salinity bias in Figure 5. Figure 6 shows for $\text{ICON-O}_{\text{UG}}$ and $\text{ICON-O}_{\text{tele}}$ the temperature and salinity biases in the Atlantic. The most distinct errors in both tracer fields occur at $\sim 60^\circ\text{N}$. This reflects biases in the processes related to the formation of NADW, such as the overflows through Denmark Strait and the Faroe Bank Channel, or deep convection. We attribute to some extend the biases in the surface and subsurface hydrography to the insufficiently tuned vertical mixing scheme. In the TKE scheme we use the parameter value $c_u = 0.1$ for both configurations (see Section 2.2.2). Later sensitivity studies with respect to this parameter have shown that this value is not optimal and that the choice $c_u = 0.2$ reduces the hydrographic biases (see also Gutjahr et al., 2021).

Compared to the results from the Ocean Model Intercomparison Study (OMIP-2; Chassignet et al., 2020) the biases of ICON-O fit well within the range of biases of the ocean models that participated in that study (cf., Figures 11 and 12 in Chassignet et al. (2020)). We remark that OMIP-2 uses a different forcing (JRA-55) and applies a different spin-up procedure.

4.3. Mixed Layer Depth

Several definitions of the mixed layer depth (MLD) are available in the literature (see e.g., the discussion in Appendix D6 of S. M. Griffies et al. (2000)). We define the MLD as the depth at which the density difference to the ocean surface is 0.125 sigma units. Figure 7 shows the monthly maximum and minimum of the MLD over the period 2010–2019. In the maximum MLD plots (left column) the North Atlantic deep water formation sites in the high latitudes are clearly identifiable, as for example, the bowl-shaped convection site in the Labrador Sea

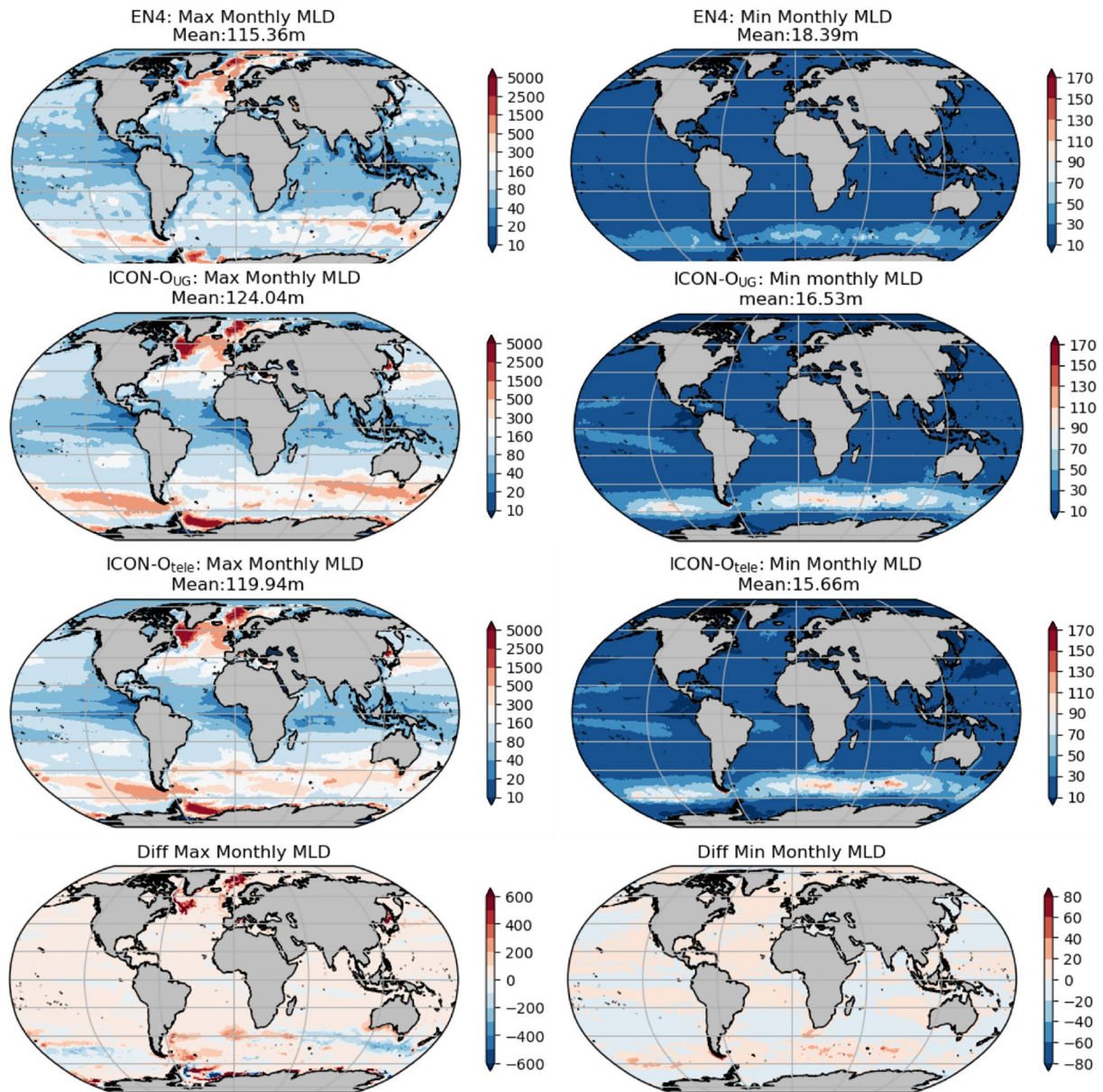


Figure 7. Mixed layer depth (MLD) from 2010 to 2019. Top row shows the EN4 data set, second row the corresponding maximum (left) and minimum (right) MLD for $\text{ICON-O}_{\text{UG}}$ and third row the maximum (left) and minimum (right) MLD of $\text{ICON-O}_{\text{tele}}$. Bottom row shows the difference $\text{ICON-O}_{\text{tele}} - \text{ICON-O}_{\text{UG}}$.

and the band of deep mixed layers in the Southern Ocean. With respect to observations of the EN4 data set (Good et al., 2013) $\text{ICON-O}_{\text{UG}}$ overestimates the MLD, the maxima and the minima are both too large. In the Labrador Sea the spatial pattern of MLD of $\text{ICON-O}_{\text{tele}}$ (top row) and $\text{ICON-O}_{\text{UG}}$ (middle row) are quite similar, the actual depth of the mixed layer differs as the difference plot in the last row of Figure 7 shows. The difference in large parts of the North Atlantic is practically zero, except for the difference in maximal MLD (left plot in the bottom row), where the maximal MLD of $\text{ICON-O}_{\text{tele}}$ exceeds clearly the maximal MLD of $\text{ICON-O}_{\text{UG}}$ in the Labrador Sea and the Greenland Sea. Overall the differences in MLD between the two configurations $\text{ICON-O}_{\text{UG}}$ and $\text{ICON-O}_{\text{tele}}$ are relatively small. This might be due to the fact that the MLD is dominated by vertical processes and forcing and to a lesser extent by the horizontal resolution. We hypothesize that the lack of tuning of the vertical mixing scheme contributes also to the difference between observed and simulated MLDs.

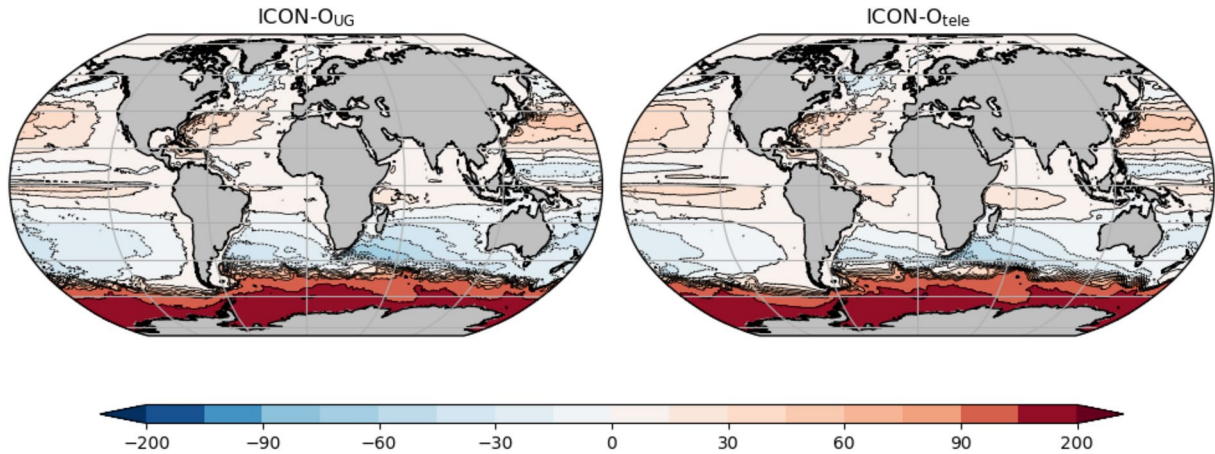


Figure 8. Barotropic streamfunction for **ICON-O_{UG}** (left) and for **ICON-O_{tele}** (right).

4.4. Transports of the Model

The barotropic stream function describes the large-scale horizontal circulation. The vertical integral from the bottom to the surface of the horizontal velocities $V := \int_{-H}^{\eta} v(z) dz$ is divergence-free, $\nabla_2 \cdot V = 0$. Therefore it can be written in terms of a two-dimensional stream function Ψ such that $V := -\nabla \times \Psi$. The barotropic stream function describes the vertically integrated volume transport, with positive values indicating a clockwise and negative values a counter clockwise flow. On unstructured grids the computation of the barotropic stream function is more involved than on latitude-longitude grids (see e.g., Sidorenko et al., 2020).

The major gyres of the large scale circulation are reproduced by **ICON-O_{UG}** (see left plot in Figure 8). In the North Atlantic the stream function shows a subtropical gyre with a maximum of about ~ 60 Sv and a subpolar gyre ~ 35 Sv. Both numbers compare well with the observational estimates of 46.0–61.0 Sv of Johns et al. (1996) for the subtropical gyre and for the subpolar gyre with the estimate 26.0–40.0 (Bacon, 1997; Bersch, 1995; Clark, 1984; Holliday et al., 2009; Lherminier et al., 2007). In the North Pacific the subtropical gyre has a maximum strength of ~ 50 Sv for **ICON-O_{UG}**.

According to Imawaki et al. (2001) the estimate is 42.0 ± 2.5 Sv. In the Southern Pacific, the subtropical gyre of **ICON-O_{UG}** has a maximum of ~ 60 Sv. The barotropic stream function also shows the Agulhas current retroflexion that provides a barrier between the Indian Ocean and the Southern Atlantic, such that the warm and salty water from the Indian Ocean enters the Atlantic mainly in form of the Agulhas rings.

Table 1 shows a list of the vertically integrated volume transport of several passages and throughflows. The simulated transport is compared to the transport estimated from observations. The volume transports simulated by **ICON-O_{UG}** agree overall quite well with the observational estimates. In the Northern Hemisphere the transports of **ICON-O_{tele}** through Denmark Strait and the Iceland Faroer Channel are slightly better than that of **ICON-O_{UG}**, while the situation is reversed for the Indonesian Throughflow, the Florida Bahamas Strait and the Mozambique Channel. We diagnose a transport of 164.9 Sv through Drake Passage for **ICON-O_{UG}** and 160.9 Sv for **ICON-O_{tele}**, which are both consistently higher than the traditional estimate of 137 ± 15 Sv by Cunningham et al. (2003) but close to the transport of 173 ± 10 Sv given by Donohue et al. (2016). The streamfunction of **ICON-O_{tele}** agrees to a large extent with the one of **ICON-O_{UG}**, in particular in the North Atlantic. This is not surprising, because the barotropic streamfunction is largely wind-driven and both model configurations are subject to the same wind field. Main differences can be seen in the Southern Hemisphere, most notably in the Indo-Pacific, where the **ICON-O_{tele}** has a much coarser resolution than **ICON-O_{UG}**.

The Drake Passage volume transport of the two configurations from 2010 to 2019 is shown in Figure 9. The transport over this period is at a relatively high level, with a simulated volume transport of **ICON-O_{UG}** that is consistently stronger than the one by **ICON-O_{tele}**. The variability of the two time series is also remarkably similar, despite the difference in resolution between the two configurations.

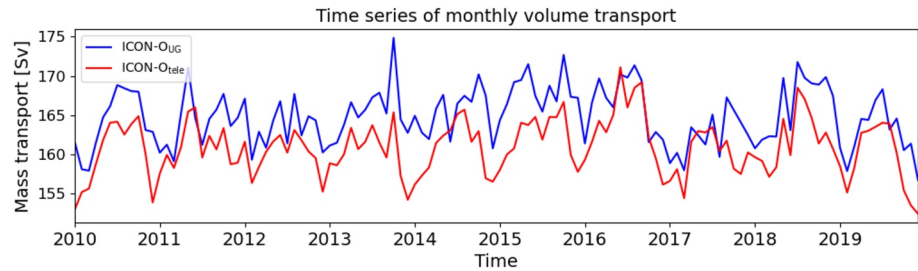


Figure 9. Time series of volume transport at Drake Passage from 2010 to 2019. The blue curve corresponds to **ICON-O_{UG}**, the red curve to **ICON-O_{tele}**.

Figure 10 shows the zonal integral of surface heat fluxes, which is also integrated meridionally from the North Pole southwards. At the equilibrium, this corresponds to the meridional heat transport by the ocean velocity field. However, our simulation is not in perfect equilibrium which explains non-negative values at the southern boundary. Nevertheless, we will refer to this quantity as meridional heat transport in the following. The meridional heat transport of **ICON-O_{UG}** and **ICON-O_{tele}** is shown in Figure 10. For the ERA5 as well as for NCEP forcing (cf., spin up in Section 3.2) the global transport (green) is decomposed into the Atlantic (red) and the Indo-Pacific (blue) contribution. The global northward transport of both configurations has a maximum at $\sim 20^{\circ}\text{N}$ of ~ 1.8 PW that agrees for both configurations reasonably well with the reanalysis based estimate from Trenberth and Caron (2001). The global minimum in the Trenberth-Caron-estimate is located at $\sim 18^{\circ}\text{S}$ and has a magnitude of ~ 1.25 PW. This estimate is reproduced by **ICON-O_{UG}**, while the **ICON-O_{tele}** minimum is located at the same position but smaller by ~ 0.3 to 0.4 PW. The local maximum at 40°S is overestimated by **ICON-O_{tele}** and its position is shifted northward. The budget of the global heat transport is not closed for both configurations, as both green curves do not approach zero in the Southern Hemisphere. This is due to the short integration time and the fact our diagnostic relies on the integrated heat flux but does not take into account the local heat content change. This affects not the position of the local minima and maxima but their magnitude. A look at the decomposition of the global heat transport in Atlantic and Pacific parts shows that in the Southern Hemisphere the Atlantic heat transport of **ICON-O_{tele}** is almost uniformly smaller by ~ 0.2 PW than the transport of **ICON-O_{UG}**, while the transports of the two configurations converge when moving northwards. This is true for the ERA5 as well as for the NCEP forced simulations. The simulated Atlantic heat transport of both configurations compares well with the estimate of 1.33 ± 0.4 PW of Johns et al. (2011). The remaining contribution to the difference between the global heat transport of **ICON-O_{tele}** and **ICON-O_{UG}** is due to the Pacific heat transport. Here, **ICON-O_{UG}** aligns with the NCEP-estimate (Trenberth & Caron, 2001) regarding the amplitude and the shape of the southward heat transport curve, while **ICON-O_{tele}** shows larger deviations such as the overestimated local minimum at $\sim 53^{\circ}\text{S}$. Since this occurs for both forcing data we attribute this to the resolution difference between **ICON-O_{UG}** and **ICON-O_{tele}** in the Pacific Ocean.

4.5. Overturning Circulation

A meridional overturning stream function with realistic transport strength and structure of the circulation cells is important for maintaining a realistic climate. The stream function is calculated by the model during runtime using the vertical velocity. The calculation of the overturning stream function follows the procedure in MPI-OM (Marsland et al., 2003) and employs an internal smoothing to filter noise from the vertical velocities. Figure 11 shows the Atlantic Meridional Overturning Circulation (AMOC) of **ICON-O_{tele}** (left) and **ICON-O_{UG}** (right).

The maximal volume transport is 18 Sv for **ICON-O_{UG}** and 20 Sv for **ICON-O_{tele}**. The depth of the upper cell of the AMOC reaches down to a depth of $\sim 3,500$ m for **ICON-O_{UG}**, for **ICON-O_{tele}** the maximal depth of the upper cell is also $\sim 3,500$ m for **ICON-O_{tele}** but toward lower latitudes the upper cell is slightly deeper than **ICON-O_{UG}**. Compared to the observations from the RAPID project (see e.g., Smeed et al., 2018) in Figure 12 we see that both overturning cells are shallower than the depth of $\sim 4,300$ m from the RAPID data. Figure 12 shows at the top the time series of the AMOC index and at the bottom the time average of the vertical profile at 26.5°N . In each of the two plots the black curves show the results from the RAPID measurements, the blue curves represent **ICON-O_{UG}** and the red ones **ICON-O_{tele}**. The colored dashed lines in the bottom plot mark two standard deviations around

Table 1
Vertical Integrated Volume Transport Through Important Passages

Section	ICON-O _{UG}	ICON-O _{tele}	Observations	References
Denmark Strait	2.9 Sv	3.0 Sv	3.2 ± 0.5 Sv	Jochumsen et al. (2017)
Iceland Faroe Channel	2.4 Sv	2.1 Sv	2.0 ± 0.2 Sv	Hansen and Ostehus (2007)
Indonesian Throughflow	13.5 Sv	9.0 Sv	15 Sv	Gordon et al. (2010)
Florida Bahamas Strait	26.9 Sv	24.0 Sv	32.1 ± 3.3 Sv	Meinen et al. (2010) and Kanzow et al. (2010)
Mozambique Channel	13.9 Sv	10.5 Sv	16 ± 13 Sv	van der Werf et al. (2010) and Ridderinkhof et al. (2010)
Drake Passage	164.8 Sv	160.9 Sv	137 ± 15 Sv 173.3 ± 10.7 Sv	Cunningham et al. (2003) Donohue et al. (2016)

the respective mean. The time series of the AMOC index shows that both **ICON-O_{UG}** as well as **ICON-O_{tele}** overestimate the transport measured by the RAPID data in the time period 2004–2019. The variability of the two configurations match the observed variability. The vertical profile shown in Figure 12 shows that **ICON-O_{UG}** overestimates the transport in the upper 2,800 m and underestimates it below this depth. We see the sign change of the transport at ~4,300 m for the RAPID data and at ~3,500 m for **ICON-O_{UG}**. The telescoping configuration **ICON-O_{tele}** shows a stronger transport than **ICON-O_{UG}** in the upper 3,000 m and a weaker one at the lower 3,000 m, it agrees better with the RAPID data in depths below 3,500 m and worse above. The change in sign of the vertical profile agrees for **ICON-O_{tele}** slightly better with RAPID than for **ICON-O_{UG}**.

ICON-O's overestimation of the overturning differs from other ocean models that often show a tendency to underestimate the transport over the whole depth (cf., AMOC profile in Figure 27 of Chassignet et al. (2020) for high-resolution and Figure 5 in Danabasoglu et al. (2014) for low resolution experiments). The strength of the overturning in ICON-O, the simulated transport at 26.5°N and also the transport through the Drake Passage are relatively strong compared to the model results shown in the OMIP-2 intercomparison (Chassignet et al., 2020) (see their Figures 15, 16 and 26).

The variety of AMOC strengths that the different models in Danabasoglu et al. (2014) exhibit, is attributed to differences in model details such as horizontal or vertical grid resolution, differences in subgrid scale parametrization or formulation of the sea-ice model. Our results show that the difference in the horizontal grid resolution between **ICON-O_{UG}** and **ICON-O_{tele}** does not create significant changes in the AMOC intensity.

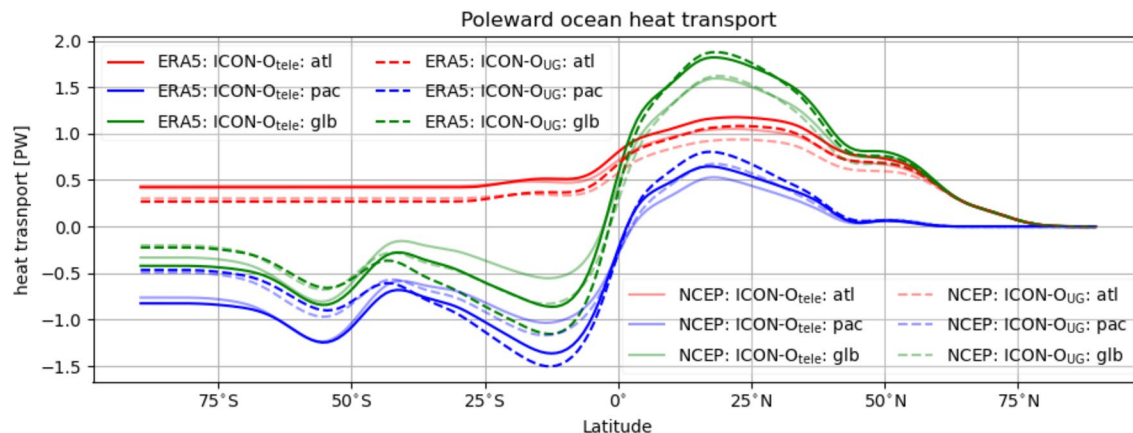


Figure 10. Simulated meridional heat transport for both configurations **ICON-O_{UG}** and **ICON-O_{tele}**, globally and basin-wise, and for the two forcing data ERA5 and NCEP.

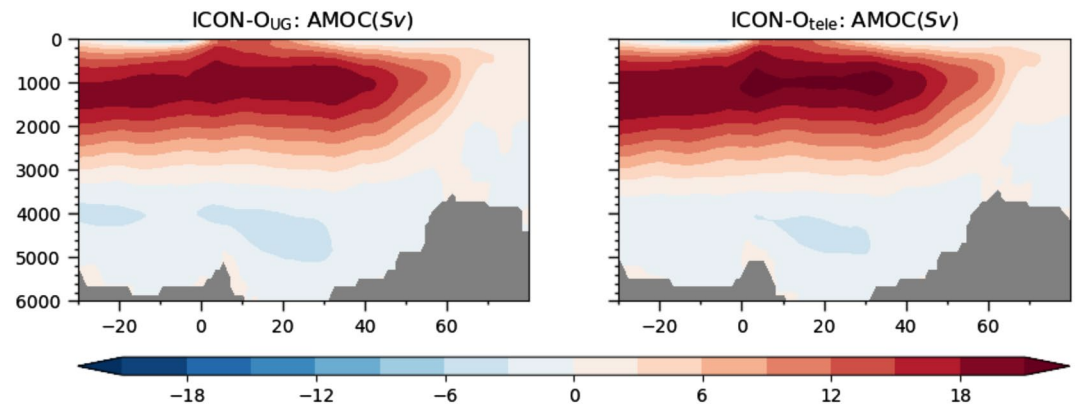


Figure 11. Atlantic meridional overturning streamfunction of **ICON-O_{UG}** (left) and **ICON-O_{tele}** (right).

4.6. Arctic and Antarctic Sea Ice

The simulated sea ice closely tracks the satellite-retrieved sea-ice concentration (Figure 13) and sea-ice area (Figure 14) in both grid configurations and in both hemispheres. The agreement is particularly good in winter, owing to the strong atmospheric temperature forcing that largely determines the location of sea ice in an ocean-only setup. Only near the ice edge, both model simulations show too high a sea-ice concentration compared to the satellite retrieval. In summer, when atmospheric temperature is close to the freezing temperature and thus compatible with both sea ice or an open ocean, **ICON-O_{tele}** and **ICON-O_{UG}** simulate too little sea ice in both hemispheres. In the Northern Hemisphere, the too low sea-ice area in summer primarily comes about by too low a sea-ice concentration of the sea-ice cover, while the overall spatial extent matches the satellite retrieval quite well (Figure 13b). The too low sea-ice concentration and the resulting additional absorption of solar radiation in summer might be one reason for the warm temperature bias in the surface waters of the Arctic Ocean (Figure 5). In the Southern Hemisphere, both model configurations lose almost all sea ice in summer. Given the substantial impact of ocean temperature on Southern Ocean sea-ice coverage, the loss of summer sea ice is potentially related to the warm temperature bias of the near-surface water (Figure 5).

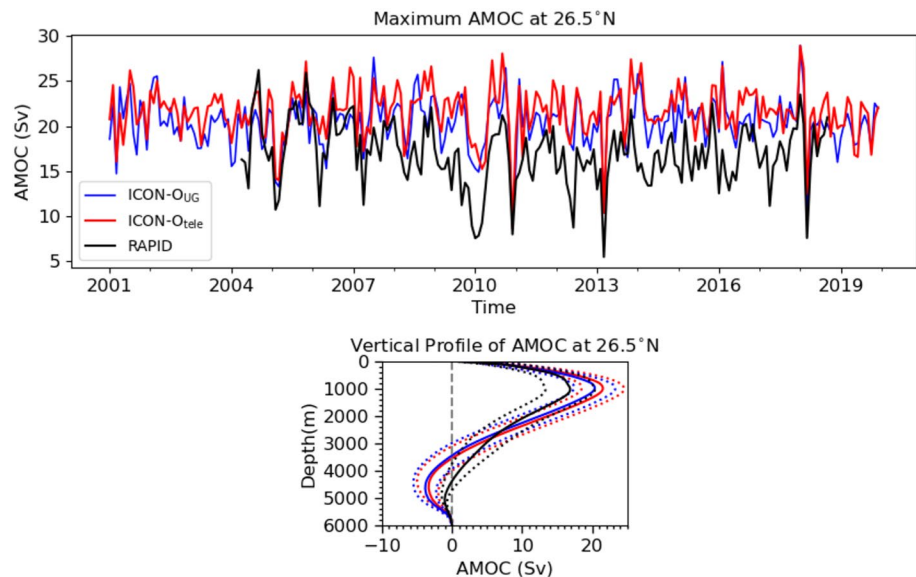


Figure 12. Top: Time series of Atlantic Meridional Overturning Circulation (AMOC) at 26.5°N. Black line shows measurements from RAPID, the blue line time series of **ICON-O_{UG}** and the red one the time series of **ICON-O_{tele}**. Bottom: Time average (2004–2019) of vertical profile at 26.5°N. The dashed lines mark two standard deviations from the mean for RAPID (black), **ICON-O_{UG}** (blue), and **ICON-O_{tele}** (red).

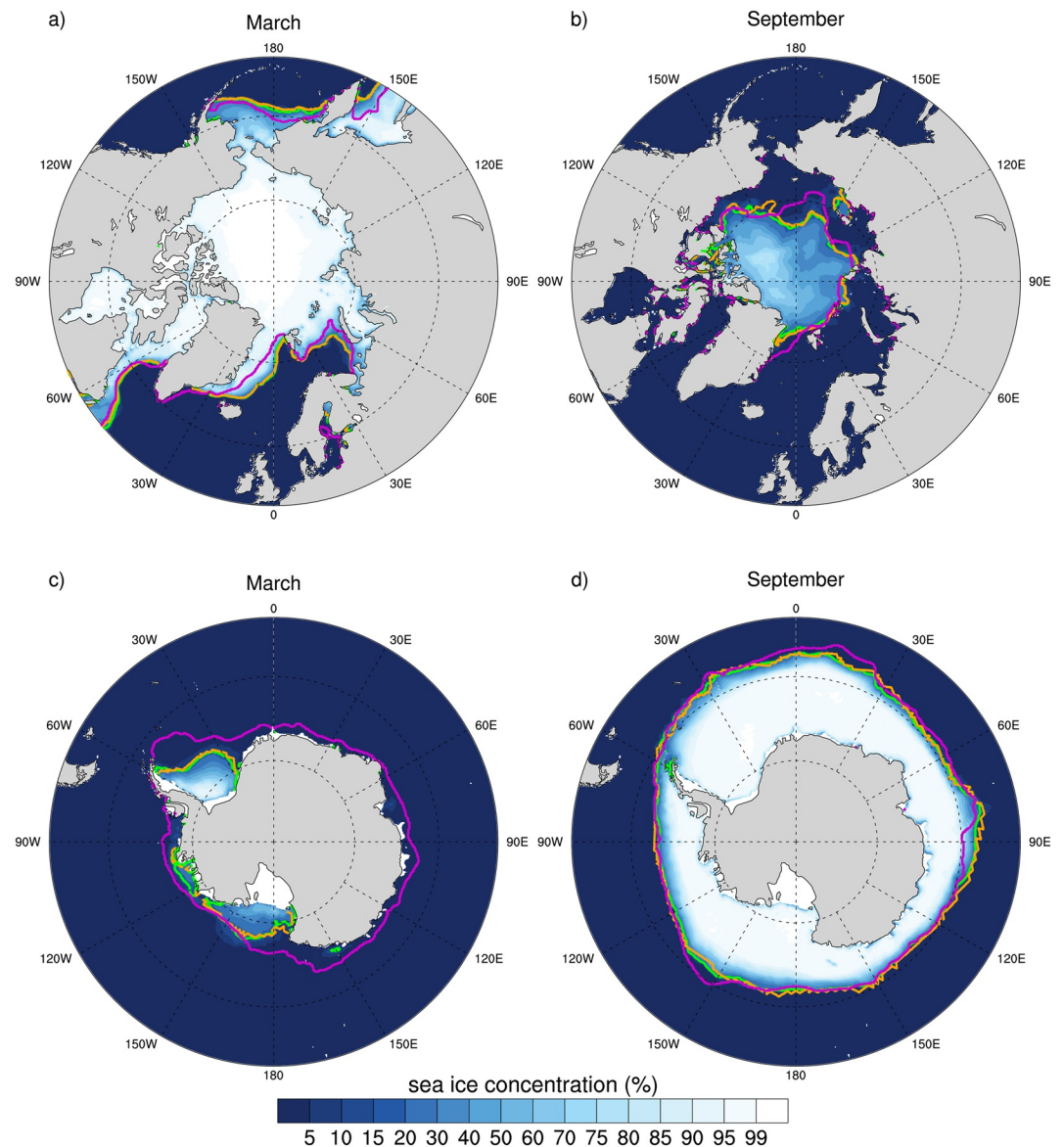


Figure 13. Time-averaged sea ice concentration (2010–2019, March and September) for (a and b) the Northern Hemisphere and (c and d) the Southern Hemisphere. Shaded in color is the sea ice concentration simulated by **ICON-O_{UG}**. Overlaid as contour lines are the 15% sea ice concentrations from **ICON-O_{UG}** (green), **ICON-O_{tele}** (orange), and from EUMETSAT OSI SAF v2.0 (OSI-450/430, magenta) (Lavergne et al., 2019).

For sea-ice thickness in the Arctic (not shown), both model configurations manage to simulate the observed spatial increase in ice thickness toward the Canadian/Greenland coast, with thicknesses in winter of about 3 m near the coastline. However, both model configurations share the common issue of having too thin winter sea ice in the central Arctic (about 1 m), and too thick sea ice at the Russian coast, with similar ice thicknesses there as on the western coastlines. In summer, both model configurations simulate a very thin ice cover throughout the Arctic, with thickness of below 0.75 m for almost all the summer sea-ice cover. The two ICON configurations show a very similar evolution of their sea-ice cover, which is not surprising given the very similar grid resolution in the high latitudes.

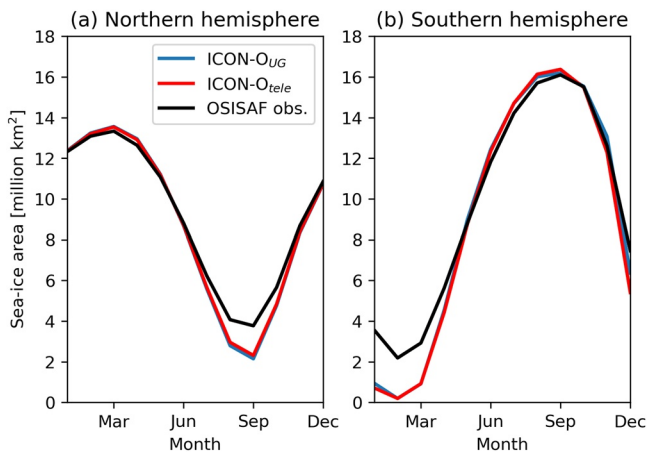


Figure 14. 2010–2019 time-averaged seasonal cycle of sea-ice area for (a) the Northern Hemisphere and (b) the Southern Hemisphere for **ICON-O_{UG}**, **ICON-O_{tele}**, and the satellite-retrieval EUMETSAT OSI SAF v2.0 (OSI-450/430) (Lavergne et al., 2019).

4.7. Variability and Local Circulation Features

In the first part of this section we study the simulated mean and variance of SSH and kinetic energy and compare these quantities with the corresponding quantities from the AVISO data (AVISO, 2021). For model as well as for observational data the variances refer to the respective temporal mean for the considered period 2010–2019. In the second part we compare the simulated velocity and temperature structure at the equatorial Pacific to observations from Johnson et al. (2002).

4.7.1. Variability of Sea Surface Height and Kinetic Energy

Figure 15 shows the bias of the mean SSH for **ICON-O_{tele}** and **ICON-O_{UG}** with respect to the mean from AVISO and it shows for both configurations the variance in SSH. The large-scale patterns of SSH are reproduced well in both simulations. Regions of larger biases are boundary currents and the Antarctic Circumpolar Current. Here, the error goes up to ~ 0.5 m. The variance of **ICON-O_{UG}** compares quite well to the variance from AVISO observations, but the minima in SSH variance in the high latitudes are overestimated by **ICON-O_{UG}**. This might be due to insufficient resolution in these regions.

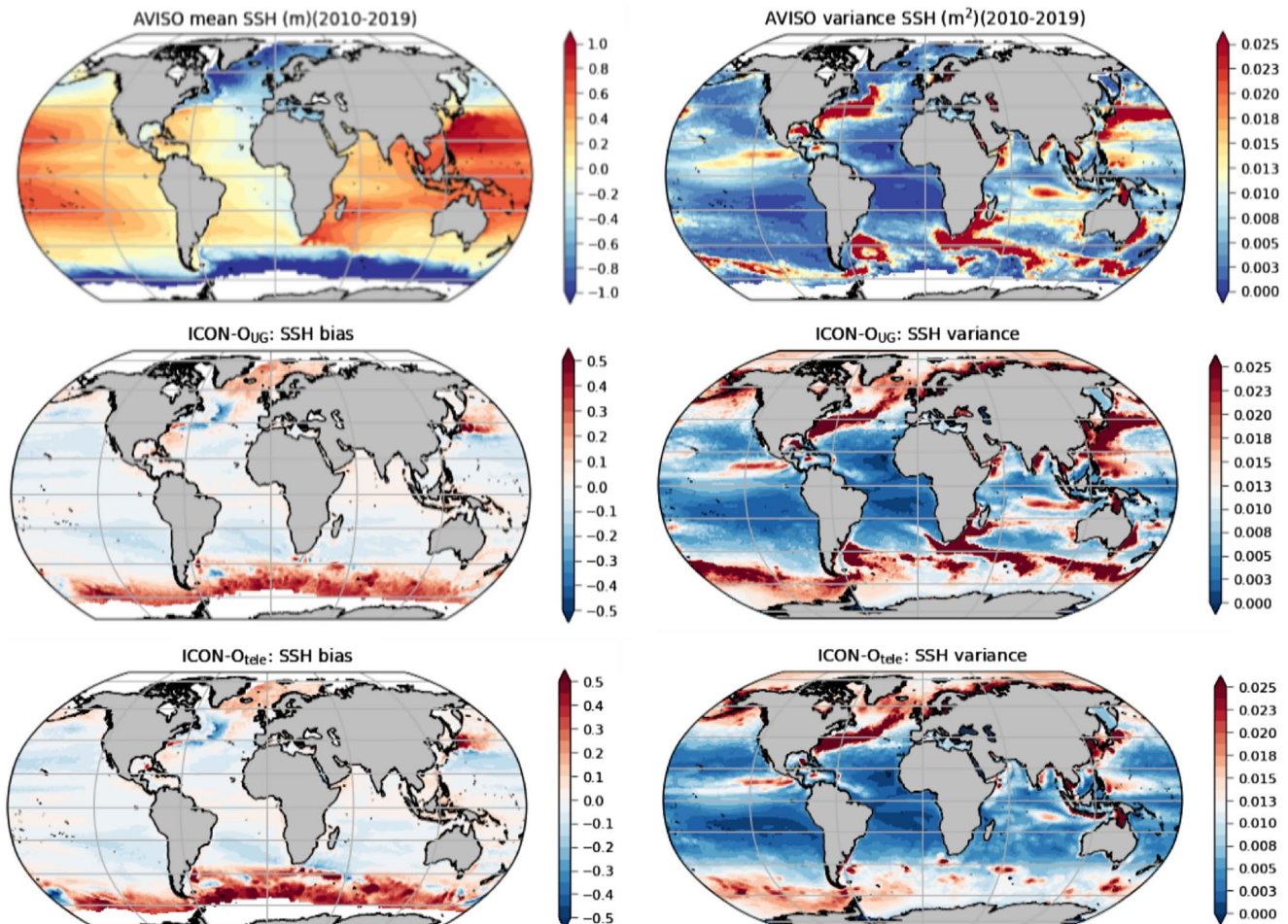


Figure 15. Mean and variance of sea-surface height from AVISO (top row), for **ICON-O_{UG}** (second row) and **ICON-O_{tele}** (bottom row).

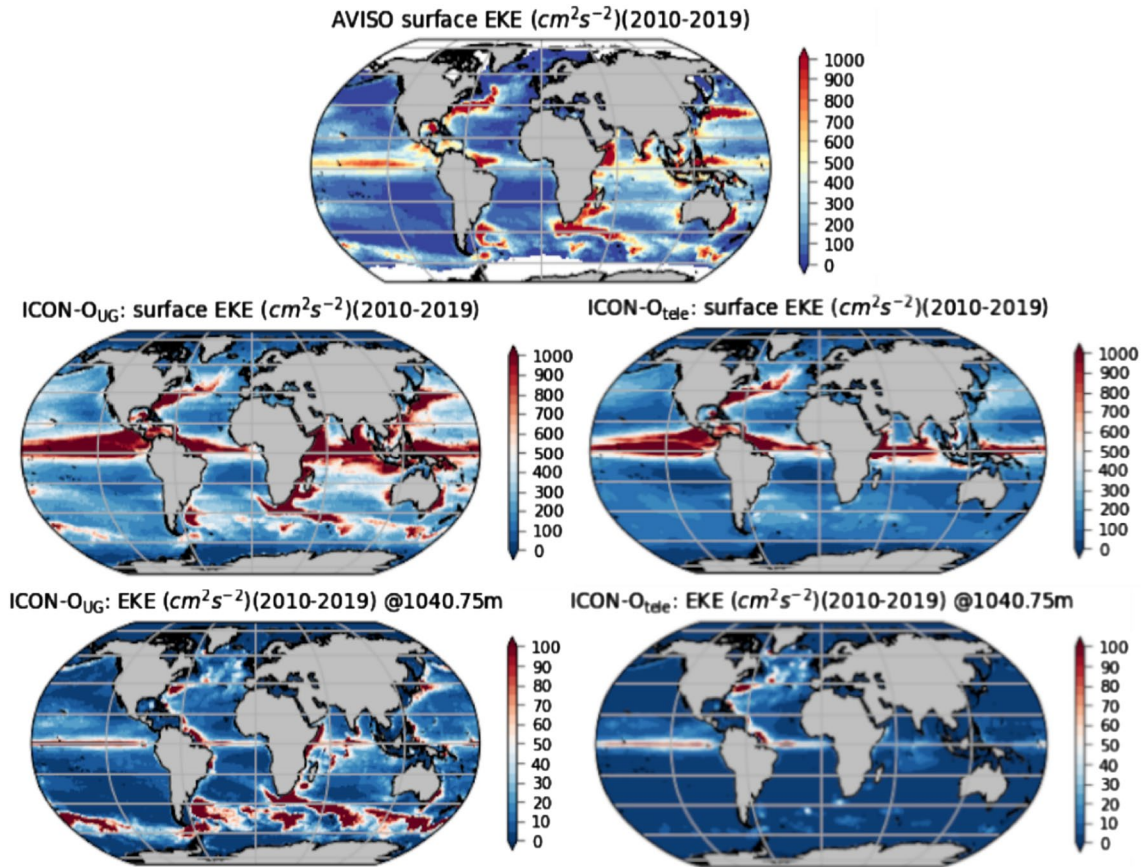


Figure 16. Eddy kinetic energy at the surface from AVISO data (top), and **ICON-O_{UG}** (second row left) and **ICON-O_{tele}** (second row right). Bottom row shows eddy kinetic energy at depth of 1,040 m for **ICON-O_{UG}** (left) and **ICON-O_{tele}** (right).

The SSH variance of **ICON-O_{tele}** in the North Atlantic and the eastern Pacific remains close to the variance of **ICON-O_{UG}**, but with increasing distance to the focal region the differences between the two simulations grow, with the most notable disagreement in the Southern Ocean, where the resolution difference is largest.

Figure 16 shows the surface eddy kinetic energy. AVISO data are on top of the figure and in the first row below are **ICON-O_{UG}** (left) and **ICON-O_{tele}** (right). The second row shows the eddy kinetic energy at depth of ~1,000 m. For the plot of the AVISO data the kinetic energy was computed via the geostrophic velocity that was derived from the SSH. The eddy component is defined as the difference between the total kinetic energy calculated from the daily geostrophic velocity outputs and the mean kinetic energy calculated from the climatological yearly means of geostrophic outputs. In **ICON-O_{UG}** the positions of regions of high eddy kinetic energy match the observations.

The surface eddy kinetic energy in the equatorial Atlantic and Pacific Ocean is for **ICON-O_{UG}** as well as for **ICON-O_{tele}** clearly overestimated relative to the AVISO estimate. This overestimation is independent of the resolution differences between both configurations. The kinetic energy in the equatorial Atlantic and Pacific Ocean is dominated by Tropical Instability Waves. Toward the equator the AVISO estimate for the surface kinetic energy becomes less reliable, because it is calculated from the observed SSH by means of geostrophy, which becomes increasingly questionable near the equator, and because the ageostrophic velocity component does not enter AVISO's kinetic energy estimate.

The eddy kinetic energy in the Southern Ocean is represented quite well by **ICON-O_{UG}**. Here, **ICON-O_{tele}** behaves differently and shows a much smaller level of surface kinetic energy than the AVISO data, a consequence of the lower resolution in the Southern Ocean. The level of eddy kinetic energy of **ICON-O_{UG}** and **ICON-O_{tele}** in the Gulf Stream region matches in principle the magnitude of the AVISO observations but the path differs from the observational data, in particular the Northwest corner is missed. The Kuroshio is simulated well in the

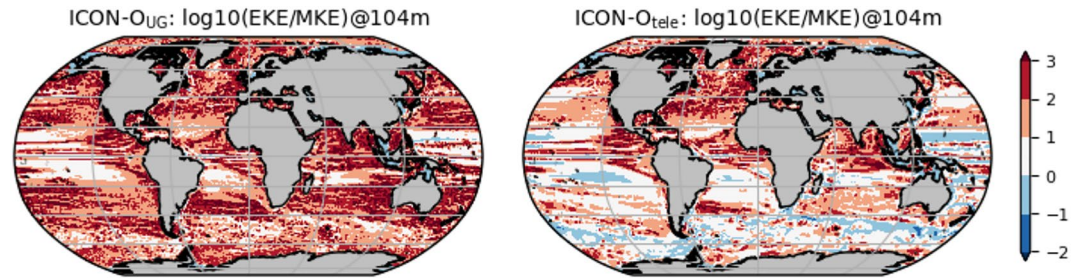


Figure 17. Ratio of mean kinetic energy and eddy kinetic energy at the surface of **ICON-O_{UG}** (left) and **ICON-O_{tele}** (right).

ICON-O_{UG} configuration but it is absent in **ICON-O_{tele}**. An analogous statement applies to the Agulhas region that is reasonably represented in **ICON-O_{UG}**, albeit with a too strong Agulhas leakage into the South Atlantic relative to AVISO, while in **ICON-O_{tele}** no elevated energy is visible and the Agulhas retroflexion is absent.

The different energetics of the two configurations in the Southern Ocean is also present in greater depths (see bottom row of Figure 16). The eddy kinetic energy in $\sim 1,000$ m shows again a high degree of similarity between **ICON-O_{UG}** and **ICON-O_{tele}** in regions of moderate difference of resolution such as the North Atlantic and the eastern part of the Pacific. In regions of large resolution difference such as the western Pacific and the Southern Ocean, we observe a weaker level of eddy kinetic energy of **ICON-O_{tele}**. Apparent in all plots is the increasing loss of variability of **ICON-O_{tele}** with increasing distance from the focal region.

Figure 17 shows the ratio of mean kinetic energy and eddy kinetic energy for **ICON-O_{UG}** and **ICON-O_{tele}**. Here, the mean kinetic energy is defined as the kinetic energy computed from the monthly mean of the velocity data. In the **ICON-O_{UG}** simulation the eddy kinetic energy exceeds everywhere the mean kinetic energy. This behavior can be expected, because **ICON-O_{UG}** resolves the first baroclinic Rossby radius over larger regions of the world's ocean than **ICON-O_{tele}**. The dominance of eddy kinetic energy over mean kinetic energy is also consistent with the analysis of the Lorenz energy cycle (see e.g., Figure 3 in von Storch et al. (2012)). The dominance of eddy over mean kinetic energy is only slightly smaller in the equatorial region. For **ICON-O_{tele}** the eddy kinetic energy generally dominates the mean kinetic energy, in particular in the North Atlantic, in the northern Indian Ocean and in the eastern part of the equatorial Pacific, but in the Southern Ocean and in parts of the Pacific Ocean we see a more mixed picture with regions where the mean kinetic energy is larger than the eddy energy.

4.7.2. Local Circulation Feature in the Pacific

The thermal structure and the velocity at a cross section of the equatorial Pacific at 110°W is shown in Figure 18. Observations of the equatorial undercurrent from Johnson et al. (2002) are shown at the first row, the second row shows results from **ICON-O_{UG}** and the third from **ICON-O_{tele}**. The zonal velocity and the temperature profile with its slightly inclined warm ellipse of **ICON-O_{UG}** agree quite well with the observations (cf., first and second row of left column of Figure 18), but the vertical decay of the observed temperature is stronger and shows a larger gradient than **ICON-O_{UG}**, while the undercurrent of **ICON-O_{tele}** (third row and left column of Figure 18) is weaker but at the right position, the negative velocity in the upper 50 m slightly north of the equator is overestimated by **ICON-O_{tele}**. Regarding the zonal velocity profile of **ICON-O_{UG}** appears slightly stronger and broader than the observations (cf., first and second row of right column of Figure 18). The inclination of the current and its near surface structure seems to be captured better by **ICON-O_{tele}**.

5. Computational Performance

In this section we give a short overview of the computational performance of the two experiments. The uniform grid setup ran on 200 nodes of the “mistral compute2” partition at the German Climate Computing Center (DKRZ). The nodes of this partition are equipped with 2×18 -core Broadwell cpus, clocked at 2.1 GHz. A combined MPI and OpenMP parallelization was employed, with 6 OpenMP threads and 6 MPI processes on each node. The turnover of this setup was 1.7 simulated years per day. The non-uniform experiment ran on 200 nodes of the compute mistral partition. The nodes of this partition are equipped with 2×12 -core Haswell cpus, clocked at 2.5 GHz. The turnover was 12 simulated years per day.

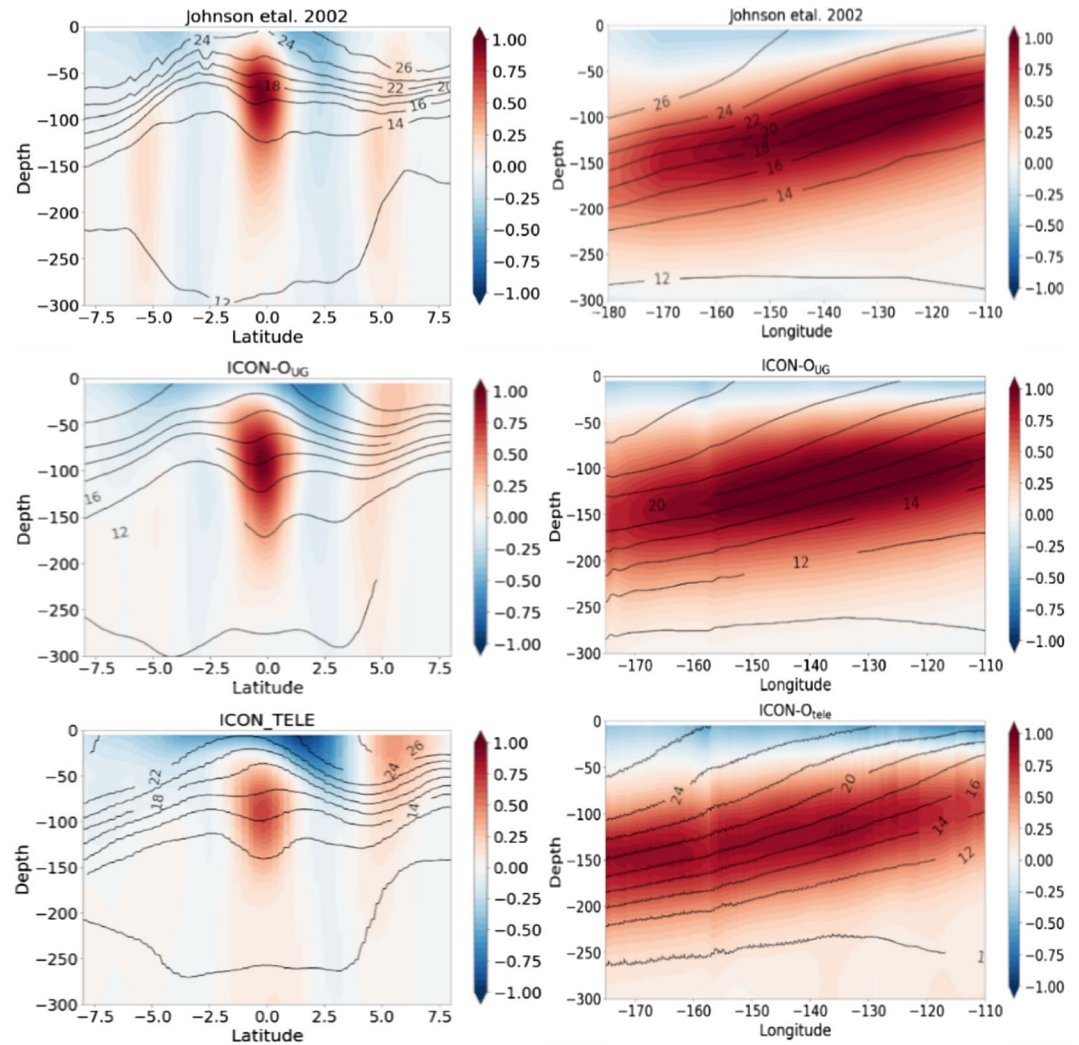


Figure 18. Cross section of zonal velocity in tropical Pacific at 110 W overlaid with temperature (right) and zonal velocities with temperature (right). The first row shows observations, second row shows **ICON-O_{UG}** and the third row **ICON-O_{tele}**.

The relative costs are given in Table 2. The most salient cost is that of output, which accounts for almost half of the runtime in the uniform setting, while 21% of the time is spent on output in the non-uniform setting. The output consists of four 3D variables for every simulated day, 90 3D variables and 86 2D variables for every simulated month. The grid size of the uniform grid is 4.4 times larger (in terms of cells) than the non-uniform, resulting in the difference in the output cost, and also in the overall performance. The output procedure used in these experiments is sequential and synchronous, forcing long waiting times when the output is called. We have recently implemented an asynchronous parallel output procedure, which we expect will significantly reduce the cost. Related to the high output cost is the diagnostics cost. The large number of diagnostic quantities require a cost of 10% for the uniform grid, and 15% for the non-uniform.

Projecting the turnover without output (we expect the relative costs to be small when using an asynchronous parallel approach in the future), but maintaining the large diagnostics cost, we would get 3.2 simulated years per day for the uniform grid, while the non-uniform gives 15 simulated years per day. Provided that the time step of the non-uniform grid is two times larger, the overall theoretical performance gain for the non-uniform grid would be 8.8

Table 2
*Relative Computational Costs for **ICON-O_{UG}** and the **ICON-O_{tele}** Setups*

Process	ICON-O_{UG}	ICON-O_{tele}
Output	0.47	0.21
Dynamics	0.12	0.20
SSH solver	0.05	0.10
Tracer advection	0.11	0.12
TKE	0.07	0.09
Ice dynamics	0.05	0.09
Diagnostics	0.10	0.15
Other	0.03	0.04

times faster. The actual speed-up is 4.7 times faster. The difference can be partially attributed to the larger cost of the solver, when a larger time step is used, and also the difference between weak and strong scaling (using 4.4 times more nodes on the non-uniform grid, relative to the uniform grid will not result in a 4.4 speed-up). In conclusion, the telescoping approach does provide an efficient way to improve the turnover of the model. A more detailed performance and scaling analysis will be undertaken in the future.

6. Discussion and Conclusion

In this work we have described two experiments carried out with ICON-O. In one model configuration, labeled **ICON-O_{UG}**, on a uniform icosahedral grid with a nominal grid resolution of ~ 10 km, and in a second configuration, termed **ICON-O_{tele}**, on a telescoping grid, with a grid resolution that ranges between 80 and 8 km in a focal area of circular shape that is located in the North Atlantic.

The message we try to convey with this work is the following:

1. **ICON-O_{UG}** provides a physically plausible simulation of the global circulation on decadal time scales.
2. **ICON-O_{tele}** delivers a circulation in the focal area that agrees on decadal time scales very well with the globally uniform model solution of **ICON-O_{UG}**.

The simulated circulation of **ICON-O_{UG}** has been analyzed with respect to important diagnostics such as biases in hydrography, simulated transports or the overturning circulation. This analysis has provided satisfactory agreement with observational measures, and the analysis has also revealed model errors that are of the same order of magnitude as those from other ocean general circulation models. We have then used **ICON-O_{UG}** as a reference solution, taken it as the best the model can deliver at a given resolution, and have studied the question how close the solution of **ICON-O_{tele}** will be in a region of interest, where grid resolution is the same as the one of **ICON-O_{UG}** but coarser outside the focal area. The encouraging result is that **ICON-O_{tele}** remains in the focal region and on decadal time scales pretty close to **ICON-O_{UG}** with respect to all diagnostics that were applied in the oceanographic analysis of **ICON-O_{UG}**. The smooth deviation of these diagnostics with increasing distance to the focal area reflects the smooth transition in resolution. Our results are of course strongly conditioned by the relatively short time scales of our simulations. On the time scales considered here we benefit first, from the smooth change of resolution in **ICON-O_{tele}** that achieves a similar resolution as **ICON-O_{UG}** over large parts of the Atlantic and second, from the fact that errors from coarsely resolved areas in **ICON-O_{tele}** need some time to travel to the focal area and affect the circulation. We have deliberately deactivated the parameterization for mesoscale eddies. This is problematic in regions such as the Southern Ocean where the **ICON-O_{tele}**-resolution does not resolve the Rossby radius such that the eddies are neither resolved nor parametrized. A sensibly tuned scale-aware eddy parametrization may reduce the differences between **ICON-O_{UG}** and **ICON-O_{tele}** in coarsely resolved regions of **ICON-O_{tele}** and prolong the time span on which the telescoping configuration provides a sufficiently good approximation to the uniform model configuration. By taking into account the model performance we can state that with **ICON-O_{tele}** we are able to simulate on decadal time scales the North Atlantic at one quarter of the cost of **ICON-O_{UG}**. We conjecture that this statement applies mutatis mutandis also to other regions of the world's ocean.

The telescoping capability is not unique to ICON-O, other unstructured grid ocean models such as FESOM and MPAS-O have similar capabilities. We speculate that the requirement to solve the dynamical equations of the ocean on an unstructured grid, without the “free lunch” of the grids orthogonality that one gets on structured grids, has stimulated the development of numerical methods that are robust under grid deformations. This robustness of the telescoping approach provides an alternative to established regionalization modeling methods such as limited-area modeling or nesting and it potentially blurs the dividing lines between regional/coastal ocean modeling at one hand and global ocean modeling at the other hand.

ICON-O forms the ocean and sea ice component of MPI-M's Earth system model ICON-ESM whose basic design is described in Jungclaus et al. (2022). The ocean biogeochemistry model HAMOCC is fully integrated into ICON-O (see Jungclaus et al., 2022; Mathis et al., 2022). The analysis carried here underscores the suitability of ICON-O for high-resolution ocean and climate modeling. A recent case study performed with the coupled ICON model at a uniform high resolution (5 km) in both the atmosphere and the ocean focuses on the interaction of a hurricane with the ocean eddy field and the hurricane's cold wake (A. Kumar et al., 2021). Another case

study using a successor of the aforementioned simulation demonstrates how katabatic storms induce dense water formation in the Irminger Sea and trigger polar lows (Gutjahr et al., 2022). This illustrates that ICON-ESM constitutes into an Earth system model that is capable of simulating the Earth system components at kilometer and subkilometer scale at global and local domains.

Appendix A: Sea Ice Model Details

As for any other ocean model, the sea ice component of **I**cosahedral **N**onhydrostatic Weather and Climate Model (ICON-O) consists of two parts, namely one describing the thermodynamic growth and decay of sea ice in a specific grid cell, and one describing the horizontal transport of sea ice from sea ice dynamics.

Sea Ice Thermodynamics. The thermodynamics of the ICON-O sea ice component is currently based on a single-category, zero-layer formulation (Semtner, 1976), reflecting the thermodynamics of the sea ice component of Max Planck Institute for Meteorology (MPI)-OM (Marsland et al., 2003). However, unlike in MPI-OM, the interface to this sea ice model is formulated such that the same thermodynamics is used for forced setups of ICON-O as described here and for coupled setups within ICON-Earth system model. Hence, the thermodynamics is split into a fast and a slow component. The fast component solves the surface-energy budget for the surface temperature of existing sea ice. It then calculates and accumulates the net heat fluxes at the sea ice surface and at the sea ice bottom for use in the slow component. Finally, the fast component updates the albedo of the sea ice surface based on surface temperature and surface type. In an uncoupled setup, the fast component is called by the ocean model at each ocean time step, whereas it is called by the atmosphere model at each atmospheric time step in a coupled setup.

The slow component, which is called by the ocean model at each ocean time step in any setup, applies the accumulated fluxes from the fast component to calculate the resulting change in ice volume in a grid cell from melting or freezing of existing ice and from the formation of new ice in open water. The latter is calculated from the net surface fluxes over open water in all grid cells. This component also calculates the change in snow thickness from precipitation and surface melting. When the freeboard of the ice becomes negative, snow-ice is formed. Finally, in the slow component of the thermodynamics, changes in ice volume are translated into changes in ice concentration and changes in ice thickness following Hibler (1979). The related parameters are used to tune the overall ice volume as described by Mauritsen et al. (2012).

Sea Ice Dynamics. The dynamics of ICON-O is based on the sea ice dynamics component of FESIM (Danilov et al., 2015). It solves the momentum equation for sea ice with an EVP rheology, following the formulation introduced by Bouillon et al. (2013). However, because ICON-O is based on a C-grid while FESIM is based on the analog of an A-grid staggering, a wrapper is needed to transfer variables between the ICON-O grid and the sea ice dynamics component.

This wrapper is based on the following steps:

1. All relevant scalars (sea ice thickness h_i , sea ice concentration C_i , snow thickness h_s , and sea surface height) are interpolated from the vertices to the cell centers and then reshaped onto the FESIM grid
2. All relevant vectors (2-D atmospheric stress terms $\vec{\tau}_a$ and 2-D sea ice velocity \vec{v}_i) are interpolated on the ICON-O grid from the cell centers to the vertices, and then reshaped onto the FESIM grid
3. The FESIM grid is rotated to have its poles lie on the equator to avoid singularities in polar regions where the sea ice exists
4. The FESIM elastic-visco-plastic solver calculates all ice velocities
5. Steps 1 to 3 are reversed to obtain velocities on ICON-O grid
6. Sea ice advection is carried out on the ICON-O grid, transporting h_i , h_s , and C_i .

This approach has a number of drawbacks. The most important ones are the numerical overhead of the required interpolation, the necessity of 3-grid-cell wide passages to allow for sea ice transport, and issues with zero sea ice velocity in grid cells neighboring land.

Data Availability Statement

The model code of **Icosahedral Nonhydrostatic Weather and Climate Model (ICON)** is available to individuals under licenses (<https://mpimet.mpg.de/en/science/modeling-with-icon/code-availability>). By downloading the ICON source code, the user accepts the licence agreement. The source code of the ICON-ESM-V1.0 used in this study, primary data, and scripts used in the analyses can be obtained from https://swiftbrowser.dkrz.de/public/dkrz_07387162e5cd4c81b1376bd7c648bb60/kornetal2021.

Acknowledgments

The authors thank the three anonymous reviewers for their constructive comments that helped to improve the paper. Open Access funding enabled and organized by Projekt DEAL.

References

- Adcroft, A., Anderson, W., Balaji, V., Blanton, C., Bushuk, M., Dufour, C. O., et al. (2019). The GFDL global ocean and sea ice model OM4.0: Model description and simulation features. *Journal of Advances in Modeling Earth Systems*, *11*(10), 3167–3211. <https://doi.org/10.1029/2019MS001726>
- Adcroft, A., & Campin, J.-M. (2004). Rescaled height coordinates for accurate representation of free-surface flows in ocean circulation models. *Ocean Modelling*, *7*(3–4), 269–284. <https://doi.org/10.1016/j.ocemod.2003.09.003>
- Androsov, A., Fofonova, V., Kuznetsov, I., Danilov, S., Rakowsky, N., Harig, S., et al. (2019). FESOM-C v.2: Coastal dynamics on hybrid unstructured meshes. *Geoscientific Model Development*, *12*(3), 1009–1028. <https://doi.org/10.5194/gmd-12-1009-2019>
- AVISO. (2021). Global ocean gridded L4 sea surface heights and derived variables reprocessed. <https://doi.org/10.48670/moi-00145>
- Bacon, S. (1997). Circulation and fluxes in the North Atlantic between Greenland and Ireland. *Journal of Physical Oceanography*, *27*(7), 1420–1435. [https://doi.org/10.1175/1520-0485\(1997\)027<1420:CAFITN>2.0.CO;2](https://doi.org/10.1175/1520-0485(1997)027<1420:CAFITN>2.0.CO;2)
- Becker, J. J., Sandwell, D. T., Smith, W. H. F., Braud, J., Binder, B., Depner, J., et al. (2009). Global bathymetry and elevation data at 30 arc seconds resolution: SRTM30_PLUS. *Marine Geodesy*, *32*(4), 355–371. <https://doi.org/10.1080/01490410903297766>
- Bersch, M. (1995). On the circulation of the northeastern North Atlantic. *Deep Sea Research Part I*, *42*(9), 1583–1607. [https://doi.org/10.1016/0967-0637\(95\)00071-D](https://doi.org/10.1016/0967-0637(95)00071-D)
- Blanke, B., & Delecluse, P. (1993). Variability of the tropical Atlantic Ocean simulated by a general circulation model with mixed layer physics. *Journal of Physical Oceanography*, *23*(7), 1363–1388. [https://doi.org/10.1175/1520-0485\(1993\)023<1363:VOTTAO>2.0.CO;2](https://doi.org/10.1175/1520-0485(1993)023<1363:VOTTAO>2.0.CO;2)
- Bouillon, S., Fichefet, T., Legat, V., & Madec, G. (2013). The elastic-viscous-plastic method revisited. *Ocean Modelling*, *71*, 2–12. <https://doi.org/10.1016/j.ocemod.2013.05.013>
- Chassignet, E. P., Yeager, S. G., Fox-Kemper, B., Bozec, A., Castruccio, F., Danabasoglu, G., et al. (2020). Impact of horizontal resolution on global ocean-sea ice model simulations based on the experimental protocols of the Ocean Model Intercomparison Project Phase 2 (OMIP-2). *Geoscientific Model Development*, *13*(9), 4595–4637. <https://doi.org/10.5194/gmd-13-4595-2020>
- Clark, R. (1984). Transport through the cape farewell-flemish cap section. *Rapp. P.-v. Reun. Cons. int. Cons. Int. Explor. Mer.*, *185*, 120–130.
- Colella, P., & Woodward, P. (1984). The piecewise-parabolic method (PPM) for gas-dynamical simulations. *Journal of Computational Physics*, *54*(1), 174–201. [https://doi.org/10.1016/0021-9991\(84\)90143-8](https://doi.org/10.1016/0021-9991(84)90143-8)
- Crüger, T., Giorgetta, M., Brokopf, R., Esch, M., Fiedler, S., Hohenegger, S., et al. (2018). ICON-A, the atmosphere component of the ICON Earth system model: II. Model evaluation. *Journal of Advances in Modeling Earth Systems*, *10*(7), 1638–1662. <https://doi.org/10.1029/2017MS001233>
- Cunningham, S., Alderson, S. G., King, B. A., & Brandon, M. A. (2003). Transport and variability of the antarctic circumpolar current in Drake Passage. *Journal of Geophysical Research*, *108*(C5), 8084. <https://doi.org/10.1029/2001JC001147>
- da Veiga, L. B., Lipnikov, K., & Manzini (2014). *The mimetic finite difference method for elliptic problems*. Springer. <https://doi.org/10.1007/978-3-319-02663-3>
- Danabasoglu, G., & Marshall, J. (2007). Effects of vertical variations of thickness diffusivity in an ocean general circulation model. *Ocean Modelling*, *18*(2), 122–141. <https://doi.org/10.1016/j.ocemod.2007.03.006>
- Danabasoglu, G., Yeager, S. G., Bailey, D., Behrens, E., Bentsen, M., Bi, D., et al. (2014). North Atlantic simulations in coordinated ocean-ice reference experiments phase II (CORE-II). Part I: Mean states. *Ocean Modelling*, *73*, 74–107. <https://doi.org/10.1016/j.ocemod.2013.10.005>
- Danilov, S. (2010). On utility of triangular C-grid type discretization for numerical modeling of large-scale ocean flows. *Ocean Dynamics*, *60*(6), 1361–1369. <https://doi.org/10.1007/s10236-010-0339-6>
- Danilov, S., Wang, Q., Timmermann, R., Iakovlev, N., Sidorenko, D., Kimmritz, M., et al. (2015). Finite-element sea ice model (FESIM), version 2. *Geoscientific Model Development*, *8*(6), 1747–1761. <https://doi.org/10.5194/gmd-8-1747-2015>
- Donohue, K., Tracey, K. L., Watts, D., Chidichimo, M., & Chereskin, T. (2016). Mean antarctic circumpolar current transport measured in Drake Passage. *Geophysical Research Letters*, *13*(22), 11760–11767. <https://doi.org/10.1002/2016GL070319>
- Eden, C., Czeschel, L., & Olbers, D. (2014). Toward energetically consistent ocean models. *Journal of Physical Oceanography*, *44*(12), 1363–1388. <https://doi.org/10.1175/JPO-D-13-0260.1>
- Engwirda, D. (2017). JIGSAW-GEO (1.0): Locally orthogonal staggered unstructured grid generation for general circulation modelling on the sphere. *Geoscientific Model Development*, *10*(6), 2117–2140. <https://doi.org/10.5194/gmd-10-2117-2017>
- Fox-Kemper, B., & Menemenlis, D. (2008). Can large eddy simulation techniques improve mesoscale rich ocean models? In M. W. Hecht & H. Hasumi (Eds.), *Ocean modeling in an eddying regime* (Vol. 177). Wiley. <https://doi.org/10.1029/177GM19>
- Gaspar, P., Grégoris, Y., & Levevre, J.-M. (1990). A simple eddy kinetic energy model for simulations of the oceanic vertical mixing' tests at station papa and long-term upper ocean study site. *Journal of Geophysical Research*, *95*(C9), 16179–16193. <https://doi.org/10.1029/JC095iC09p16179>
- Gates, L. D., Hagemann, S., & Golz, C. (1993). *Observed historical discharge data from major rivers for climate model validation* (Tech. Rep., Vol. 307). Max Planck Institute for Meteorology.
- Gent, P. R., & McWilliams, J. C. (1990). Isopycnal mixing in ocean circulation models. *Journal of Physical Oceanography*, *20*(1), 150–155. [https://doi.org/10.1175/1520-0485\(1990\)020%3C0150:MIOCM%3E2.0.CO;2](https://doi.org/10.1175/1520-0485(1990)020%3C0150:MIOCM%3E2.0.CO;2)
- Giorgetta, M., Brokopf, R., Crüger, T., Esch, M., Fiedler, S., Helmert, J., et al. (2018). ICON-A, the atmosphere component of the ICON Earth system model: I. Model description. *Journal of Advances in Modeling Earth Systems*, *10*(7), 1613–1637. <https://doi.org/10.1029/2017MS001242>
- Good, S. A., Martin, M. J., & Rayner, N. (2013). EN4: Quality controlled ocean temperature and salinity profiles and monthly objective analyses with uncertainty estimates. *Journal of Geophysical Research: Oceans*, *118*(12), 6704–6716. <https://doi.org/10.1002/2013JC009067>
- Gordon, A., Sprintall, J., Aken, H. V., Susanto, R., Wijffels, S., Molcard, R., et al. (2010). The Indonesian throughflow during 2004–2006 as observed by the instant program. *Dynamics of Atmospheres and Oceans*, *50*(2), 115–128. <https://doi.org/10.1016/j.dynatmoce.2009.12.002>

- Griffies, S. (1998). The Gent-McWilliams skew flux. *Journal of Physical Oceanography*, 28(5), 831–841. [https://doi.org/10.1175/1520-0485\(1998\)028<0831:TGMSEF>2.0.CO;2](https://doi.org/10.1175/1520-0485(1998)028<0831:TGMSEF>2.0.CO;2)
- Griffies, S., Gnanadesikan, A., Pacanowski, R., Larichev, V. D., Dukowicz, J., & Smith, R. (1998). Isoneutral diffusion in a z-coordinate model. *Journal of Physical Oceanography*, 28(5), 805–830. [https://doi.org/10.1175/1520-0485\(1998\)028<0805:IDIAZC>2.0.CO;2](https://doi.org/10.1175/1520-0485(1998)028<0805:IDIAZC>2.0.CO;2)
- Griffies, S. M., Adcroft, A., & Hallberg, R. W. (2020). A primer on the vertical Lagrangian-remap method in ocean models based on finite volume generalized vertical coordinates. *Journal of Advances in Modeling Earth Systems*, 12(10), e2019MS001954. <https://doi.org/10.1002/2016GL070319>
- Griffies, S. M., Boening, C., Bryan, F. O., Chassignet, E. P., Gerdes, R., Hasumi, H., et al. (2000). Developments in ocean climate modelling. *Ocean Modelling*, 2(3–4), 123–192. [https://doi.org/10.1016/S1463-5003\(00\)00014-7](https://doi.org/10.1016/S1463-5003(00)00014-7)
- Gutjahr, O., Brüggemann, N., Haak, H., Jungclaus, J., Putrasahan, D., Lohmann, K., & von Storch, J.-S. (2021). Comparison of ocean vertical mixing schemes in the Max Planck Institute Earth System Model (MPI-ESM1.2). *Geoscientific Model Development*, 14(5), 2317–2349. <https://doi.org/10.5194/gmd-14-2317-2021>
- Gutjahr, O., Jungclaus, J. H., Brüggemann, N., Haak, H., & Marotzke, J. (2022). Air-sea interactions and water mass transformation during a katabatic storm in the Irminger Sea. *Journal of Geophysical Research: Oceans*, 127(5), e2021JC018075. <https://doi.org/10.1029/2021JC018075>
- Hallberg, R. (2013). Using a resolution function to regulate parameterizations of oceanic mesoscale eddy effects. *Ocean Modelling*, 72, 92–103. <https://doi.org/10.1016/j.ocemod.2013.08.007>
- Hansen, B., & Ostehus, S. (2007). Faroe bank channel overflow 1995–2005. *Progress in Oceanography*, 75(4), 817–856. <https://doi.org/10.1016/j.pocean.2007.09.004>
- Heikes, R., & Randall, D. (1995a). Numerical integration of the shallow-water equations on a twisted icosahedral grid. Part I: Basic design and results of tests. *Monthly Weather Review*, 123(6), 1862–1880. [https://doi.org/10.1175/1520-0493\(1995\)123<3C1862:NIOTSW%3E2.0.CO;2](https://doi.org/10.1175/1520-0493(1995)123<3C1862:NIOTSW%3E2.0.CO;2)
- Heikes, R., & Randall, D. (1995b). Numerical integration of the shallow-water equations on a twisted icosahedral grid. Part II: Detailed description of the grid and analysis of numerical accuracy. *Monthly Weather Review*, 123(6), 1881–1887. [https://doi.org/10.1175/1520-0493\(1995\)123<3C1862:NIOTSW%3E2.0.CO;2](https://doi.org/10.1175/1520-0493(1995)123<3C1862:NIOTSW%3E2.0.CO;2)
- Hersbach, H., Bell, B., Berrisford, P., Biavati, G., Horanyi, A., Sabater, J. M., et al. (2018). ERA5 hourly data on single levels from 1979 to present (Copernicus Climate Change Service (C3S) Climate Data Store (CDS)). <https://doi.org/10.24381/cds.adbb2d47>
- Hibler, W. D. (1979). A dynamic thermodynamic sea ice model. *Journal of Physical Oceanography*, 9(4), 817–846. [https://doi.org/10.1175/1520-0485\(1979\)009<3C0815:ADTSIM%3E2.0.CO;2](https://doi.org/10.1175/1520-0485(1979)009<3C0815:ADTSIM%3E2.0.CO;2)
- Hoch, K., Petersen, M. R., Brus, S. R., Engwirda, D., Roberts, A. F., Rosa, K., & Wolfram, P. J. (2020). MPAS-ocean simulation quality for variable-resolution North American coastal meshes. *Journal of Advances in Modeling Earth Systems*, 12(3), 1–23. <https://doi.org/10.1029/2019MS001848>
- Holliday, N. P., Bacon, S., Allen, J., & McDonagh, E. L. (2009). Circulation and transport in the western boundary currents at Cape Farewell, Greenland. *Journal of Physical Oceanography*, 39(8), 1854–1870. <https://doi.org/10.1175/2009JPO4160.1>
- Imawaki, S., Uchida, H., Ichikawa, H., Fukasawa, M., Umatani, S., & Group, A. (2001). Satellite altimeter monitoring the kuroshio transport south of Japan. *Geophysical Research Letters*, 28(1), 17–20. <https://doi.org/10.1029/2000GL011796>
- Jackett, D. R., McDougall, T. J., Wright, D. G., & Griffies, S. M. (2006). Algorithms for density, potential temperature, conservative temperature, and the freezing temperature of seawater. *Journal of Atmospheric and Oceanic Technology*, 23(12), 1709–1728. <https://doi.org/10.1175/JTECH1946.1>
- Jochumsen, K., Moritz, M., Nunes, N., Quadfasel, D., Larsen, K. M. H., Hansen, B., et al. (2017). Revised transport estimates of the Denmark Strait overflow. *Journal of Geophysical Research: Oceans*, 122(4), 3434–3450. <https://doi.org/10.1002/2017JC012803>
- Johns, W., Baringer, M., Beal, L., Cunningham, S., Kanzow, T., Bryden, H., et al. (2011). Continuous, array-based estimates of Atlantic Ocean heat transport at 26.5°N. *Journal of Climate*, 24(10), 2429–2449. <https://doi.org/10.1175/2010JCLI3997.1>
- Johns, W., Shay, T., Bane, J., & Watts, D. (1996). Gulf Stream structure, transport, and recirculation near 68°W. *Journal of Geophysical Research*, 100(C1), 817–838. <https://doi.org/10.1029/94JC02497>
- Johnson, G., Sloyan, B., Kessler, W., & McTaggart, K. (2002). Direct measurements of upper ocean currents and water properties across the tropical Pacific during the 1990s. *Progress in Oceanography*, 52(1), 31–61. [https://doi.org/10.1016/S0079-6611\(02\)00021-6](https://doi.org/10.1016/S0079-6611(02)00021-6)
- Jungclaus, J., Lorenz, S. J., Schmidt, H., Brovkin, V., Brüggemann, N., Chegini, F., et al. (2022). The ICON Earth system model version 1.0. *Journal of Advances in Modeling Earth Systems*, 14(4), e2021MS002813. <https://doi.org/10.1029/2021MS002813>
- Kalnay, E., Kanamitsu, M., Kistler, R., Collins, W., Deaven, D., Gandin, L., et al. (1996). The NCEP/NCAR 40-year reanalysis project. *Bulletin of the American Meteorological Society*, 77(3), 437–471. [https://doi.org/10.1175/1520-0477\(1996\)077<0437:TNYRP>2.0.CO;2](https://doi.org/10.1175/1520-0477(1996)077<0437:TNYRP>2.0.CO;2)
- Kanzow, T., Cunningham, S., Johns, W. E., Hirschi, J.-M., Marotzke, J., Meinen, M. O. B. C., et al. (2010). Seasonal variability of the Atlantic Meridional Overturning Circulation at 26.5°N. *Journal of Climate*, 23(21), 5678–5698. <https://doi.org/10.1175/2010JCLI3389.1>
- Korn, P. (2017). Formulation of an unstructured grid model for global ocean dynamics. *Journal of Computational Physics*, 339, 525–552. <https://doi.org/10.1016/j.jcp.2017.03.009>
- Korn, P. (2018). A structure-preserving discretization of ocean parametrizations on unstructured grids. *Ocean Modelling*, 132, 73–90. <https://doi.org/10.1016/j.ocemod.2018.10.002>
- Korn, P., Brüggemann, N., Gutjahr, O., Haak, H., Ramme, L., & Singh, V. (2022). A conservative ocean-sea-ice model including phase transitions. In preparation.
- Korn, P., & Danilov, S. (2017). Elementary dispersion analysis of some mimetic discretizations on triangular C-grids. *Journal of Computational Physics*, 330, 156–172. <https://doi.org/10.1016/j.jcp.2016.10.059>
- Korn, P., & Linardakis, L. (2018). A conservative discretizations of the shallow-water equations on triangular grids. *Journal of Computational Physics*, 375, 871–900. <https://doi.org/10.1016/j.jcp.2018.09.002>
- Kumar, A. U., Brüggemann, N., Smith, R. K., & Marotzke, J. (2021). Response of a tropical cyclone to a subsurface ocean eddy and the role of boundary layer dynamics. *Quarterly Journal of the Royal Meteorological Society*, 148(742), 378–402. <https://doi.org/10.1002/qj.4210>
- Large, W., Danabasoglu, G., Doney, C., & McWilliams, J. C. (1997). Sensitivity to surface forcing and boundary layer mixing in a global ocean model: Annual-mean climatology. *Journal of Physical Oceanography*, 27(11), 2417–2447. [https://doi.org/10.1175/1520-0485\(1997\)027<2418:STSFAB>2.0.CO;2](https://doi.org/10.1175/1520-0485(1997)027<2418:STSFAB>2.0.CO;2)
- Large, W. G., McWilliams, J., & Doney, S. (1994). Oceanic vertical mixing: A review and a model with a nonlocal boundary layer parameterization. *Review of Geophysics*, 21(4), 363–403. <https://doi.org/10.1029/94RG01872>
- Lavergne, T., Sørensen, A. M., Kern, S., Tonboe, R., Notz, D., Aaboe, S., et al. (2019). Version 2 of the EUMETSAT OSI SAF and ESA CCI sea-ice concentration climate data records. *The Cryosphere*, 13(1), 49–78. <https://doi.org/10.5194/tc-13-49-2019>
- Lherminier, P., Mercier, H., Gourcuff, C., Alvarez, M., Bacon, S., & Kermabon, C. (2007). Transports across the 2002 Greenland-Portugal Ovide section and comparison with 1997. *Journal of Geophysical Research*, 112(C7), C07003. <https://doi.org/10.1029/2006JC003716>

- Lipnikov, K., Manzini, G., & Shashkov, M. (2014). Mimetic finite difference method. *Journal of Computational Physics*, 257, 1163–1227. <https://doi.org/10.1016/j.jcp.2013.07.031>
- Logemann, K., Linardakis, L., Korn, P., & Schrum, C. (2021). Global tide simulations with ICON-O: Testing the model performance on highly irregular meshes. *Ocean Dynamics*, 21(1), 43–57. <https://doi.org/10.1007/s10236-020-01428-7>
- Madec, G., Bourdallé-Badie, R., Chanut, J., Clementi, E., Coward, A., Ethé, C., et al. (2022). NEMO ocean engine. In Scientific Notes of IPSL Climate Modelling Center (v4.2, Number 27). <https://doi.org/10.5281/zenodo.6334656>
- Maier-Reimer, E., Mikolajewicz, U., & Hasselmann, K. (1993). Mean circulation of the Hamburg LSG OGCM and its sensitivity to the thermohaline surface forcing. *Journal of Physical Oceanography*, 23(4), 731–757. [https://doi.org/10.1175/1520-0485\(1993\)023<0731:MCOTHL>2.0.CO;2](https://doi.org/10.1175/1520-0485(1993)023<0731:MCOTHL>2.0.CO;2)
- Marsland, S. J., Bindoff, N. L., Williams, G., & Budd, W. F. (2004). Modeling water mass formation in the Mertz Glacier Polynya and Adélie Depression, east Antarctica. *Journal of Geophysical Research*, 109(C11), C11003. <https://doi.org/10.1029/2004JC002441>
- Marsland, S. J., Haak, H., Jungclaus, J. H., Latif, M., & Röske, F. (2003). The Max-Planck-Institute global ocean/sea ice model with orthogonal curvilinear coordinates. *Ocean Modelling*, 5(2), 97–127. [https://doi.org/10.1016/S1463-5003\(02\)00015-X](https://doi.org/10.1016/S1463-5003(02)00015-X)
- Mathis, M., Logemann, K., Maerz, J., Lacroix, F., Hagemann, S., Chegini, F., et al. (2022). A seamless connection of the open and coastal ocean in marine carbon cycle. *Journal of Advances in Modeling Earth Systems*. <https://doi.org/10.1029/2021MS002789>
- Maurer, V., Früh, B., Giorgetta, M. A., Steger, C., Brauch, J., Schnur, R., & Zängl, G. (2022). *Domain nesting in ICON-A and its application to AMIP experiments with regional refinement* (Tech. Rep.). German Weather Service DWD. https://doi.org/10.5676/DWD_pub/nwv/icon_008
- Mauritsen, T., Stevens, B., Roeckner, E., Crueger, T., Mesch, T. C., Giorgetta, M., et al. (2012). Tuning the climate of a global model. *Journal of Advances in Modeling Earth Systems*, 4(3), 3167–3211. <https://doi.org/10.1029/2012MS000154>
- Mehlmann, C., Danilov, S., Losch, M., Lemieux, J., Hutter, N., Richter, T., et al. (2021). Simulating linear kinematic features in viscous-plastic sea ice models on quadrilateral and triangular grids. *Journal of Advances in Modeling Earth Systems*, 13(11), e2021MS002523. <https://doi.org/10.1029/2021MS002523>
- Mehlmann, C., & Korn, P. (2021). Sea-ice dynamics on triangular grids. *Journal of Computational Physics*, 428, 110086. <https://doi.org/10.1016/j.jcp.2020.110086>
- Meinen, C. S., Baringer, M. O., & Garcia, R. F. (2010). Florida current transport variability: An analysis of annual and longer-period signals. *Deep-Sea Research*, 57(7), 835–846. <https://doi.org/10.1016/j.dsr.2010.04.001>
- Mikolajewicz, U., Sein, D., Jacob, D., Kahl, T., Podzun, R., & Semmler, T. (2005). Simulating arctic sea ice variability with a coupled regional atmosphere-ocean-sea ice model. *Meteorologische Zeitschrift*, 14(6), 793–800. <https://doi.org/10.1127/0941-2948/2005/0083>
- Olbers, D., & Eden, C. (2013). A global model for the diapycnal diffusivity Induced by Internal gravity waves. *Journal of Physical Oceanography*, 43(8), 1759–1779. <https://doi.org/10.1175/JPO-D-12-0207.1>
- Pacanowsky, R., & Philander, S. (1981). Parameterization of vertical mixing in numerical models of tropical oceans. *Journal of Physical Oceanography*, 11, 1443–1451. [https://doi.org/10.1175/1520-0485\(1981\)011<1443:POVMIN>2.0.CO;2](https://doi.org/10.1175/1520-0485(1981)011<1443:POVMIN>2.0.CO;2)
- Redi, M. H. (1982). Oceanic isopycnal mixing by coordinate rotation. *Journal of Physical Oceanography*, 12(10), 1154–1158. [https://doi.org/10.1175/1520-0485\(1982\)012<1154:OIMBCR>2.0.CO;2](https://doi.org/10.1175/1520-0485(1982)012<1154:OIMBCR>2.0.CO;2)
- Ridderinkhof, H., van der Werf, P., Ullgren, J., van Aken, H., van Leeuwen, P., & Ullgren, P. (2010). Seasonal and interannual variability in the Mozambique Channel from moored current observations. *Journal of Geophysical Research*, 115(C6), C06010. <https://doi.org/10.1029/2009JC005619>
- Ringler, T., Petersen, M., Higdon, R., Jacobsen, D., Jones, P. W., & Maltrud, M. (2013). A multi-resolution approach to global ocean modeling. *Ocean Modelling*, 69, 211–232. <https://doi.org/10.1016/j.ocemod.2013.04.010>
- Röske, F. (2006). A global heat and freshwater forcing dataset for ocean models. *Ocean Modelling*, 11(3–4), 235–297. <https://doi.org/10.1016/j.ocemod.2004.12.005>
- Satoh, M. (2013). *Atmospheric circulation dynamics and general circulation models* (Vol. 1). Springer. <https://doi.org/10.1007/978-3-642-13574-3>
- Scholz, P., Sidorenko, D., Danilov, S., Wang, Q., Koldunov, N., Sein, D., & Jung, T. (2022). Assessment of the Finite-volume Sea ice-Ocean Model (FESOM2.0) – Part 2: Partial bottom cells, embedded sea ice and vertical mixing library CVMIX. *Geoscientific Model Development*, 15(12), 4875–4899. <https://doi.org/10.5194/gmd-15-335-2022>
- Scholz, P., Sidorenko, D., Gurses, O., Danilov, S., Koldunov, N., Wang, Q., et al. (2019). Assessment of the Finite-volume Sea ice-Ocean Model (FESOM2.0) – Part 1: Description of selected key model elements and comparison to its predecessor version. *Geoscientific Model Development*, 12(11), 4875–4899. <https://doi.org/10.5194/gmd-12-4875-2019>
- Schulzweida, U. (2021). CDO user guide – Version 2.0.5. Retrieved from <https://code.mpimet.mpg.de/projects/cdo/embedded/cdo.pdf>
- Sein, D., Danilov, S., Biastoch, A., Durgadoo, J., Sidorenko, D., Harig, S., & Wang, Q. (2019). Designing variable ocean model resolution based on the observed ocean variability. *Journal of Advances in Modeling Earth Systems*, 8(2), 904–916. <https://doi.org/10.1002/2016MS000650>
- Semtner, A. J. (1976). A model for the thermodynamic growth of sea ice in numerical investigations of climate. *Journal of Physical Oceanography*, 6(3), 379–389. [https://doi.org/10.1175/1520-0485\(1976\)006<0379:AMFTTG>2.0.CO;2](https://doi.org/10.1175/1520-0485(1976)006<0379:AMFTTG>2.0.CO;2)
- Sidorenko, D., Danilov, S., Koldunov, N., Scholz, P., & Wang, Q. (2020). Simple algorithms to compute meridional overturning and barotropic streamfunctions on unstructured meshes. *Geoscientific Model Development*, 13(7), 3337–3345. <https://doi.org/10.5194/gmd-13-3337-2020>
- Smeed, D. A., Josey, S. A., Beaulieu, C., Johns, W. E., Moat, B. I., Frajka-Williams, E., et al. (2018). The North Atlantic Ocean is in a state of reduced overturning. *Geophysical Research Letters*, 45(3), 1527–1533. <https://doi.org/10.1002/2017gl076350>
- Steele, M., Morley, R., & Ermold, W. (2001). PHC: A global ocean hydrography with a high quality Arctic Ocean. *Journal of Climate*, 14(9), 2079–2087. [https://doi.org/10.1175/1520-0442\(2001\)014<2079:PAGOHW>2.0.CO;2](https://doi.org/10.1175/1520-0442(2001)014<2079:PAGOHW>2.0.CO;2)
- Stuhne, G. R., & Peltier, W. B. (2006). A robust unstructured grid discretization for 3-dimensional hydrostatic flows in spherical geometry: A new numerical structure for ocean general circulation modeling. *Journal of Computational Physics*, 213(2), 704–729. <https://doi.org/10.1016/j.jcp.2005.08.031>
- Stuhne, G. R., & Peltier, W. B. (2009). An unstructured C-grid based method for 3-D global ocean dynamics: Free-surface formulations and tidal test cases. *Journal of Computational Physics*, 28(1–3), 97–105. <https://doi.org/10.1016/j.ocemod.2008.11.005>
- Tomita, H., Satoh, M., & Goto, K. (2002). An optimization of icosahedral grid modified by spring dynamics. *Journal of Computational Physics*, 183(1), 579–613. <https://doi.org/10.1006/jcph.2002.7193>
- Tomita, H., Tsugawa, M., Satoh, M., & Goto, K. (2001). Shallow water model on a modified icosahedral geodesic grid by using spring dynamics. *Journal of Computational Physics*, 174(2), 579–613. <https://doi.org/10.1006/jcph.2001.6897>
- Trenberth, K. E., & Caron, J. M. (2001). Estimates of meridional atmosphere and ocean heat transports. *Journal of Climate*, 14(16), 3433–3443. [https://doi.org/10.1175/1520-0442\(2001\)014<3433:EOMAAO>2.0.CO;2](https://doi.org/10.1175/1520-0442(2001)014<3433:EOMAAO>2.0.CO;2)
- UNESCO. (1981). The practical salinity scale 1978 and the international equation of state of seawater 1980. UNESCO Technical Papers in Marine Science 36.

- UNESCO. (2010). IOC, SCOR and IAPSO, 2010: The international thermodynamic equation of seawater – 2010: Calculation and use of thermodynamic properties. Intergovernmental Oceanographic Commission, Manuals and Guides No. 56.
- van der Werf, P. M., van Leeuwen, P. J., Ridderinkhof, H., & de Ruijter, W. P. M. (2010). Comparison between observations and models of the Mozambique channel transport: Seasonal cycle and eddy frequencies. *Journal of Geophysical Research*, *115*(C2), C02002. <https://doi.org/10.1029/2009JC005633>
- Veneziani, M., Maslowski, W., Lee, Y. J., Angelo, G. D., Osinski, R., Petersen, M. R., et al. (2022). An evaluation of the E3SMv1-Arctic Ocean/sea ice regionally refined model. *Geoscientific Model Development*, *15*(7), 3133–3160. <https://doi.org/10.5194/gmd-12-4875-2019>
- von Storch, J.-S., Eden, C., Fast, I., Haak, H., Hernandez-Deckers, D., Maier-Reimer, E., et al. (2012). An estimate of the Lorenz energy cycle for the world ocean based on the 1/10° STORM/NCEP simulation. *Journal of Physical Oceanography*, *42*(12), 2185–2205. <https://doi.org/10.1175/JPO-D-12-079.1>
- Wan, H., Giorgetta, M. A., Zängl, G., Restelli, M., Majewski, D., Bonaventura, L., et al. (2013). The ICON-1.2 hydrostatic atmospheric dynamical core on triangular grids – Part 1: Formulation and performance of the baseline version. *Geoscientific Model Development*, *6*(3), 735–763. <https://doi.org/10.5194/gmd-6-735-2013>
- Wolff, J. O., Maier-Reimer, E., & Legutke, S. (1997). *The Hamburg ocean primitive equation model hope* (Tech. Rep.). Deutsches Klimarechenzentrum.
- Wolfram, P. J., & Fringer, O. B. (2013). Mitigating horizontal divergence “checker-board” oscillations on unstructured triangular C-grids for nonlinear hydrostatic and nonhydrostatic flows. *Ocean Modelling*, *69*, 64–78. <https://doi.org/10.1016/j.ocemod.2013.05.007>
- Zalesak, S. (1979). Fully multidimensional flux-corrected transport algorithms for fluids. *Journal of Computational Physics*, *31*(3), 335–362. [https://doi.org/10.1016/0021-9991\(79\)90051-2](https://doi.org/10.1016/0021-9991(79)90051-2)
- Zängl, G., Reinert, D., Ripodas, P., & Baldauf, M. (2015). The ICON (ICOsahedral Non-hydrostatic) modelling framework of DWD and MPI-M: Description of the non-hydrostatic dynamical core. *Quarterly Journal of the Royal Meteorological Society*, *141*(687), 563–579. <https://doi.org/10.1002/qj.2378>